Early Development of 3D-Printed Implants for Mandibular Condyle Regeneration

By

Jean Remy Salash

B.S., Chemical Engineering, University of Kansas

Submitted to the Bioengineering Graduate Program and the Graduate Faculty of the University of Kansas in partial fulfillment of the requirements for the degree of Master of Science.

Committee Members:

_____

Dr. Arghya Paul, Committee Chair

_____

Dr. Michael Detamore

_____

Dr. Brian Andrews

Date Defended: March 8, 2017

The thesis committee for Jean Remy Salash certifies that this is the approved version of the following thesis:

Early Development of 3D-Printed Implants for Mandibular Condyle Regeneration

_____

Dr. Arghya Paul, Committee Chair

Date Approved: March 8, 2017

Abstract

In recent years, three-dimensional (3D) printing has opened up unprecedented opportunities in the field of tissue engineering, providing researchers with more precise control over the macro- and microstructural characteristics of scaffolds. Through the layer-by-layer patterning of material, 3D printing enables the production of increasingly sophisticated scaffolds that aim to mimic the complexities of native extracellular matrix so as to instruct resident cells to synthesize the envisioned tissue. Motivated by the recognized need for tissue-engineering solutions for mandibular condyle regeneration, the objective of this thesis was to develop patient-specific scaffolds with discrete yet integrated osteo- and chondroinductive regions using two 3D printing techniques, direct ink writing (DIW) and fused deposition modeling (FDM). Toward this objective, chondroinductive hydrogel 'ink' comprised of pentenoate-modified hyaluronic acid (PHA) and decellularized cartilage (DCC) microparticles was designed for DIW using a customized syringe-based extrusion tool. Notably, DCC microparticles were found to enhance the rheological properties of the hydrogel 'ink' for 3D printing, and accordingly improved the resolution of the 3D-printed hydrogel structures. In addition, PHA/DCC hydrogel was shown to simulate chondrogenic differentiation of seeded bone marrow-derived mesenchymal stem cells *in vitro* as evidenced by elevated expression levels of SOX9, a chondrogenic gene, demonstrating its potential for cartilage tissue engineering applications. In parallel, osteoinductive monofilament feedstock for FDM composed of polycaprolactone and hydroxyapatite nanopowder was made in-house. Computed tomography and computer-aided design (CAD) modeling techniques were used to create digital models of the bone and cartilage-promoting regions of the scaffold, with anatomical geometries and regional interconnected pore structures for translation into an early prototype. However, due to several technical constraints, multi-

material scaffold production was unfeasible. To advance scaffold development, a 3D printing system with higher resolution and positioning accuracy, and more advanced extrusion tools would be required to improve the co-deposition of hydrogel ink and thermoplastic-based filament to successfully produce the osteochondral scaffold design.

Acknowledgements

I would like to express my sincere gratitude to my committee members, parents and friends. Thank you to my co-advisors, Dr. Paul and Dr. Detamore, for your mentorship, to Dr. Andrews for your support through the University of Kansas Medical Center, and to Dr. Berkland for your guidance and encouragement. Immeasurable thanks are owed to my parents for your unfailing support. This would not have been possible without you! To my friends including all of my lab mates, thanks for journeying with me through this wild adventure. This work was made possible through the financial support of the Department of Plastic Surgery at the University of Kansas Medical Center.

Table of Contents

Chapter 1: Introduction

The long-term objective of this thesis was to develop patient-specific implants or scaffolds composed of osteo- and chondroinductive biomaterials using combined three-dimensional (3D) printing technologies to replace and regenerate the mandibular condyle. Direct ink writing (DIW) and fused deposition modeling (FDM) techniques were employed using an open-source 3D printer equipped with customized tool heads to enable the computer-driven assembly of hydrogels and thermoplastic-based monofilaments into complex, hybrid structures. The scaffold was designed to have well-defined yet integrated tissue-specific regions to promote the formation of osteochondral tissue similar to that found in the mandibular condyle. The dimensions and contours of each region were informed by medical images, and an internal pore structure was introduced using computer-aided design (CAD) techniques to enable endogenous cell infiltration and tissue ingrowth.

However, since biomaterials must meet stringent biological, structural and processing requirements for utilization in 3D printing for tissue engineering applications, the development of 'printable' biomaterials continues to remain a significant challenge.[1] Therefore, biocompatible and cell-instructive biomaterials were also developed to manufacture viable scaffolds with the customized 3D printing system. Acellular hyaluronic acid (HA)-based hydrogel 'ink' enriched with decellularized cartilage (DCC) microparticles was optimized for printing the cartilage region of the scaffold, and novel polycaprolactone and hydroxyapatite composite monofilament was fabricated for printing the bone region. Biomaterials were selected based on clinical translation and commercialization considerations so as to avoid the need for scaffold pre-culture or the incorporation of growth factors to bypass the regulatory challenges associated with the approval of combination products by the Food and Drug Administration.

Due to the interdependency of technical and biomaterial constraints, the scope of this thesis was relegated in large part to chondroinductive hydrogel ink design, optimization and characterization, though early prototyping of the osteochondral implant was also performed. To this end, the first specific aim was to devise a method to print hydrogel and to evaluate the printing capabilities and rheological properties of pre-crosslinked HA-based hydrogels with various molecular weights of HA, polymer contents and concentrations of DCC microparticles. The second aim was to assess the mechanical properties of 3D-printed HA-based hydrogels as well as the *in vitro* response of bone marrow-derived mesenchymal stem cells cultured on the hydrogels. The third specific aim was to design and manufacture 3D-printed osteochondral implants from medical computed tomography (CT) data with user-defined pore architectures by spatially patterning hydrogel 'ink' and thermoplastic-based monofilament to construct anatomically-relevant, cell-instructive scaffolds for mandibular condyle regeneration.

Chapter 2 proposes a set of clinical indications for engineered temporomandibular joint components established by a group of field experts including clinicians, surgeons, and researchers. In particular, the potential indications for bioengineered mandibular condyle implants, including irreparable trauma, developmental or acquired deformities in skeletally immature individuals, hyperplasia and documented metal sensitivities, provided the motivation to pursue the development of a tissue engineering-based solution to improve treatment outcomes for these patient populations.

Chapter 3 addresses the first and second aim of designing and characterizing a chondroinductive hydrogel for 3D printing. The rheological properties and printability of pentenoate-modified HA (PHA) hydrogel 'ink' with various concentrations of DCC were evaluated. Mechanical testing was performed on 3D-printed and mold-casted PHA/DCC

hydrogels to assess the effects of DCC concentration and the method of fabrication on the structural integrity of the hydrogel. Furthermore, the chondroinductive potential of crosslinked PHA/DCC hydrogels was evaluated *in vitro*. The results from these studies were vital in advancing toward the third aim focused on CAD-driven scaffold production through the co-deposition of hydrogel by DIW and thermoplastic composite material by FDM.

Chapter 4 addresses the third aim of designing and manufacturing patient-specific osteochondral scaffolds for mandibular condyle regeneration using dual extrusion techniques. This chapter describes the scaffold design process from CT image acquisition to the generation of a digital model, and outlines the work done to date in pursuit of scaffold production using combined DIW and FDM techniques. Additionally, this chapter describes the difficulties and challenges encountered in 3D printing with novel biomaterials, and explains the limitations that need to be overcome or bypassed in order to realize this objective.

Chapter 5 provides concluding remarks and summarizes the findings of this thesis. Recommendations for future work are also provided along with a full list of constraints that must be overcome to produce hybrid scaffolds by the co-deposition of hydrogel 'ink' and thermoplastic composite monofilament.

Chapter 2: Potential Indications for TMJ Tissue Engineering in TMJ Surgery*

ABSTRACT

Purpose: Musculoskeletal tissue engineering has advanced to the stage where it has the capability to engineer temporomandibular joint (TMJ) anatomical components. Unfortunately, there is a paucity of literature identifying specific indications for the use of TMJ tissue engineering solutions. The objective of this paper is to establish an initial set of indications and contraindications for the use of engineered tissues for replacement of TMJ anatomical components.

Findings: There was consensus among the authors that the management of patients requiring TMJ reconstruction as the result of 1) irreparable condylar trauma, 2) developmental or acquired TMJ pathology in skeletally immature patients, 3) hyperplasia, and 4) documented metal hypersensitivities may be indications for bioengineered condyle/ramus TMJ components. There was consensus that Wilkes Stage III internal derangement may be an indication for utilization of a bioengineered TMJ disc, or possibly even a disc-like, bioengineered "fossa liner". However, there was some controversy as to whether TMJ arthritic disease (e.g., osteoarthritis) and reconstruction after failed alloplastic devices should be indications. Further research is required to determine whether tissue engineered TMJ components could be a viable option for such cases. Contraindications for the use of bioengineered TMJ components may include TMJ patients with multiple failed surgeries, parafunctional oral habits, chronic TMJ infection, TMJ rheumatoid arthritis and ankylosis unless the underlying pathology could be resolved.

* Published as Salash, J. R., Hossameldin, R. H., Almarza, A. J., Chou, J. C., McCain, J. P., Mercuri, L. G., Wolford, L. M., Detamore, M. S. (2016). Potential Indications for Tissue Engineering in Temporomandibular Joint Surgery. *Journal of Oral and Maxillofacial Surgery*, *74*(4), 705-711.

Conclusions: Biomedical engineers must appreciate the specific indications that may warrant TMJ bioengineered structures, so that they avoid developing technologies in search of problems that may not exist for patients and clinicians. Instead, they should first focus on identifying and understanding the problems that need resolution, and then tailor technologies to address those specific situations. The aforementioned indications and contraindications are designed to serve as a guide to the next generation of tissue engineers in their strategic development of technologies to address specific clinical issues.

INTRODUCTION

Temporomandibular joint (TMJ) disorders, characterized by pain and/or reduced mandibular function, affect millions of individuals nationwide. To improve mandibular function and symptom relief in selected individuals with severe, debilitating, end-stage disorders, TMJ reconstruction using autogenous grafts or alloplastic implants is often required. Bioengineered tissue replacements with the potential to restore health and functionality to the joint may provide an attractive alternative to conventional management options.

As the field of tissue engineering advances, the potential to replace TMJ anatomical components is becoming a reality.[2-5] To assist researchers in the development of viable technologies, direction from clinicians is required to identify the clinical situations where bioengineering management strategies may be advantageous. A series of four TMJ Bioengineering Conferences in 2006,[4] 2009, 2012, and 2014, have succeeded in advancing directives to bioengineers from clinicians for the development and use of TMJ tissue engineered structures. These conferences in many cases successfully identified objectives and potential pitfalls associated with tissue engineering technology. However, to date, there is a paucity of

literature identifying the specific patient indications justifying TMJ tissue engineering solutions. Just as there are a set of accepted indications and contraindications for alloplastic total TMJ replacement,[6] the objective of this paper aims to establish an initial set of indications and contraindications for the use of engineered tissue for the replacement of TMJ anatomical components.

The purpose of the current paper is not to suggest or propose design strategies or specific clinical management options. The indications and contraindications proposed clarify for the first time patient populations that may benefit from tissue engineering management strategies. Furthermore, this paper will help motivate new and emerging bioengineers and clinicians to engage in research to improve TMJ replacement outcomes for patients.

Where there was consensus among the authors versus where there were differing points of view will be noted. These agreements and points of controversy both emphasize the need for caution and careful investigation and collaboration with clinicians as the TMJ bioengineering community advances the field over the next decade.

INDICATIONS FOR MANDIBULAR CONDYLE AND RAMUS BIOENGINEERING

Bioengineered implants with the ability to regenerate the mandibular condyle and ramus could improve the quality of care for many patients requiring surgical intervention or total replacement of the TMJ.[7] One hurdle for bioengineering in the TMJ field is the success of alloplastic total joint replacement,[8] as surgeons may be hesitant to abandon a familiar and successful approach in favor of new technology. Nevertheless, implantation of a bioengineered mandibular condyle/ramus may hold great promise in the management of patients requiring TMJ reconstruction as the result of 1) irreparable condylar trauma, 2) developmental or acquired TMJ

pathology in skeletally immature patients, 3) hyperplasia, and 4) documented metal hypersensitivities.

Condylar Trauma

In patients with irreparable condylar trauma (severe anatomically disruptive intracapsular/extracapsular injuries) where conventional surgical intervention is not possible, bioengineered implants may be used to reproduce the anatomical form of injured mandibular components. Presently, off-the-shelf, or stock alloplastic TMJ devices are useful in such cases requiring immediate surgical intervention. However, bioengineered TMJ implants could also be used to correct deformities resulting from the inadequate repair or insufficient management of the primary injury (e.g., malunion caused by condylar or subcondylar fracture). Malposition of the condylar head is a common complication that occurs secondary to extracapsular fractures; so, in these cases, biological reconstruction may be advocated to re-establish proper mandibular posterior vertical dimension of occlusion.

Skeletally Immature Patients

Skeletally immature patients requiring TMJ reconstruction may benefit from bioengineered replacements, which potentially have the ability to grow with the patient. Patients with developmental disorders, such as hemifacial microsomia and Treacher Collins syndrome, may be suitable candidates for bioengineered implants. In addition, these implants may be useful in the restoration of occlusal vertical dimension in skeletally immature patients who have acquired defects involving the TMJ.

Classically, pathologic, developmental, and functional disorders affecting the TMJ in skeletally immature patients have been reconstructed with autogenous tissues.[9-14] In theory, in these patients, autogenous allografts will grow with the patient. However, often this so-called growth potential has been reported to be unpredictable or to result in ankylosis. These complications can occur either as the result of the allograft and/or fixation failure or because of the uncooperative nature of the young patient with physical therapy after reconstruction.[15, 16]

Recent studies have even questioned the necessity for using an autogenous graft to restore and maintain mandibular growth.[17, 18] Long-term reports of mandibular growth in children whose TMJs were reconstructed with autogenous costochondral grafts demonstrated that excessive growth on the treated side occurred in 54% of the 72 cases examined and growth equal to that on the opposite side occurred in only 38% of the cases.[19-24] Furthermore, Peltomäki *et al*.,[25-27] in an investigation of mandibular growth after costochondral grafts, supported previous experiments with regard to the inability of the graft to adapt to the growth velocity of the new environment.

In summary, it is reasonable to consider careful examination of the use of bioengineered tissue in in skeletally immature patients. Again, problems with autogenous grafts in skeletally immature patients include graft failure, unpredictable growth, ankylosis, and potential for donor-site morbidity. Furthermore, the orthopedic literature has extensively reported success with alloplastic devices in improving the quality of life of such patients with severe anatomical and functional joint disorders.[9]

Hyperplasia

Condylar hyperplasia and hypertrophy are other proposed indications for bioengineered condyle implantation in skeletally immature patients. These implants may be used to replace areas of excessive or disproportionate cellular growth to halt the disease process and reconstruct the functional anatomy of the joint. However, precautions must be taken to ensure that all of the diseased tissue is excised and that relapse is avoided. The underlying disease process and cause of the inherent imbalance of extracellular matrix synthesis, and degradation in the condyle would need to be better understood to ensure clinical success.

Metal Hypersensitivities

Lastly, total TMJ alloplastic joint replacement candidates exhibiting metal hypersensitivities[28, 29] may benefit from bioengineered implants. Prior to alloplastic joint reconstruction, skin patch testing or the more sensitive lymphocyte transformation testing have been recommended.[30] These tests can help to identify which implant materials affect atopy in hypersensitive individuals. If a material hypersensitivity can be documented, then bioengineered implants may be desirable to avoid adverse immune reactions and device failure.

Focal mandibular condylar defects may also be considered a potential indication;[31] although consensus among the authors for this indication was not reached since these abnormalities are not frequently observed in the condyle or ramus. There may be a limited set of patients who would benefit from focal defect repair, for example those with osteophytes that must be removed,[32] although the need is not likely large enough to motivate companies to seek FDA approval for use in this application. In contrast, there is a significant need to develop bioengineering solutions for focal cartilage defect regeneration in other synovial joints such as

the knee,[33] where isolated cartilage injuries are highly prevalent. This marked difference highlights the importance of understanding the therapeutic needs specific to the TMJ to develop treatments with clinical relevance. Though the need for focal defect repair in the mandible may be negligible, bioengineered implants or plugs may be viable agents for the treatment of chondral lesions in the articular eminence.

INDICATIONS FOR ARTICULAR DISC BIOENGINEERING

Surgical implantation of bioengineered articular discs is a proposed management option for patients with unsalvageable discs caused by injury or disease, as well as for patients with Wilkes stage III and IV internal derangements or disc displacements without reduction.[34] In addition, disc implants may be an effective complement to bioengineered condyles to better approximate the functional structures of the TMJ in patients requiring total bioengineered joint reconstruction.[4]

Bioengineering solutions may also be desirable to manage perforations in the articular disc,[35-38] although there is controversy surrounding whether perforations occur most commonly within the disc itself[39] or whether they occur more commonly in the attachment tissues surrounding the disc. It must be noted that with perforations there are often other associated degenerative changes in the TMJ,[40] and in those cases, managing the perforation itself may be valuable but insufficient without addressing any pathologic condylar changes. Furthermore, there is a question as to whether successfully mending a perforation would directly improve function or prevent further progressive degeneration of articulating cartilage and bone.

In cases where the articular disc alone is in need of repair, bioengineered disc implantation may be indicated. Common etiological factors that contribute to disc deterioration

are mechanical injury, infection and degenerative joint disease. At present, a discectomy without subsequent disc replacement is the accepted procedure for the management of irreparable articular discs.[41] However, discectomies are controversial and their success is highly debatable.[42] Bioengineered disc replacements may therefore offer a promising alternative to exceed current management outcomes.[42] However, surgical implantation with attachment of the disc to surrounding structures, and the ability of the disc to mechanically support articulation are significant concerns that must be addressed by both bioengineers and clinicians. Since the disc translates with jaw motion and articulates with both the articular eminence and the superior surface of the condyle, reestablishing proper disc position and function may be unrealistic. An implant that attaches to and lines the fossa may be an alternative viable solution to bioengineered disc replacement.

Internal derangements are another proposed indication for bioengineered disc replacement. However, replacement of the disc alone may only be desirable for Wilkes Stage III and IV internal derangements. Internal derangements are a result of mechanical dysfunction and signs of underlying TMJ pathology. If the underlying pathology is not diagnosed and corrected prior to disc replacement, the bioengineered implant may suffer the same fate as the original disc. Therefore, bioengineered fossa liners may be preferred over true bioengineered disc implants, as such a liner would provide a smooth surface for condylar movements during function, and may prevent degeneration of the condyle due to overload associated with progression to Wilkes Stages IV and V despite the underlying pathology.

Disc replacements in combination with bioengineered mandibular components may be implanted as a unit when a total joint replacement is indicated. This implantable unit may obviate the need for autogenous reconstruction of the condyle and interpositional temporalis muscle.

Composite disc and condyle bioengineered replacements would be advantageous for management of adolescent idiopathic condylar resorption and reactive arthritis, degenerative conditions in which the disc and condyle degenerate past the point of being salvageable.

Patients may be candidates for bioengineered disc replacements or focal repair unless they have an unresolved underlying pathology such as advanced degenerative joint disease, or persistent parafunctional habits.[43] Synovitis and chondromalacia may or may not be contraindications for bioengineered implants, consensus was not achieved among the authors for these two indications.

CONTRAINDICATIONS FOR BIOENGINEERED TMJ TISSUES

The most common complication of TMJ trauma is ankylosis (bone overgrowth), a condition where biological reconstruction may be inadvisable. The surgical management goals for TMJ ankylosis include restoring function, reducing pain, and preventing recurrence. Bioengineered implants may likely suffer the same fate as autogenous grafts, which often fail due to recurrence of the ankylosis. Therefore, alloplastic TMJ replacement, as it is in orthopedics in other joints, is the management option of choice for TMJ ankylosis.[44]

There was some controversy in discussions amongst authors concerning the use of bioengineered tissues in an ankylosis environment. On one hand, autologous costochondral grafts have been employed in treating select ankylosis cases with varying degrees of success,[45-48] which may pave the way for bioengineered tissue solutions for carefully selected ankylosis patients. However, there is significant skepticism at this time for the use of tissue engineering approaches in managing ankylosis given that it may unintentionally facilitate the recurrence of the ankylosis by stimulating bone overgrowth.

Bioengineered TMJ implants also may not be indicated for patients who have undergone multiple failed TMJ surgeries or been exposed to failed alloplastic TMJ devices.[44, 49] The viability of bioengineered implants relies heavily on both the degree of vascularization within the implant and the reactivity of the surrounding environment. In patients who have undergone multiple operations,[38, 49, 50] the formation of thick scar tissue is unavoidable and can impede vascular infiltration, leading to poor implant survival and performance.

Bioengineered implants may further be contraindicated for use in reactive or inflammatory environments such as rheumatoid arthritis,[51] where the underlying autoimmune disease may destroy the regenerated tissue. An unresolved local infection would also be a contraindication to implanting a TMJ bioengineered device.[52]

DISCUSSION

Due to continued advances in the field of tissue engineering, the use of bioengineered implants to regenerate joints is on the horizon. As the creation of viable tissue replacements comes closer to becoming a reality, the TMJ clinical community must clearly identify specific indications and contraindications for the use of such components. It is imperative that researchers in this field understand the needs of the clinicians who manage TMJ patients. This understanding will ensure that the solutions developed are both useful and beneficial to TMJ patients, and have long-term safety and efficacy.

The authors have identified four primary TMJ patient populations potentially suitable for bioengineered condylar implants. These include the management of patients requiring TMJ reconstruction as the result of 1) irreparable condylar trauma, 2) developmental or acquired TMJ pathology in skeletally immature patients, 3) hyperplasia, and 4) documented metal

hypersensitivities. The authors felt that the use of bioengineered implants were a lower priority in patients with focal condylar defects. However, there may be use for an implant to regenerate focal defects located in the articular eminence.

One of the limiting factors for the use of bioengineered tissue would be the presence of innate TMJ pathological conditions, such as degenerative joint disease (osteoarthritis), where the use of bioengineered TMJ constructs may be of questionable value. For example, low inflammatory osteoarthritis resulting from acute or chronic TMJ trauma may be a good indication for reconstruction with bioengineered materials since no underlying local or systemic immune response exists. However, disorders such as high inflammatory rheumatoid arthritis may limit the effectiveness of biological restorations since systemic immune responses would attack the bioengineered implant in the same manner as the native condyle unless the underlying disease is managed successfully and systemically. Since bioengineered tissue is susceptible to the same mechanisms of disease as the natural TMJ, prior to considering bioengineered implants, the etiology and pathology of the disease process present must be understood. Therefore, presently, alloplastic TMJ replacement is considered the management option of choice for patients with end-stage low and high inflammatory TMJ pathology.

Complications that could be associated with the use of bioengineered tissue in the management of TMJ pathology include all of the complications reported for both autogenous and alloplastic TMJ TJR.[5, 44, 49, 52] The most common being infection, heterotopic ossification and ankylosis, unpredictable growth, and persistent post-implantation pain. However, material hypersensitivity could be avoided.

In the future, if bioengineered implants achieve long-term success, the need for autogenous grafts may be eliminated. The use of bioengineered devices would reduce the

number of surgical sites, eliminate donor site morbidity, and minimize the severity of the procedure and recovery time.

The authors felt there were conditions that may contraindicate the use of TMJ bioengineered devices, such as parafunctional oral habits, chronic local TMJ infection, TMJ ankylosis, end-stage diseases such as rheumatoid arthritis, multiply operated patients, and patients previously exposed to failed alloplastic devices.

An engineering strategy may not be useful for TMJ replacement in the multiply operated patient because scar tissue forms with each surgery, which may affect angiogenesis in the bioengineered device due to limited diffusion. This may account for the clinical observation that free autogenous tissue grafts, such as cartilage, costochondral and sternoclavicular grafts often fail in cases of multiply operated patients or those with extreme anatomical architectural discrepancies resulting from pathology.[6] Unless angiogenesis can be induced, bioengineered implants may not be able to support cellular activity and may thus be prone to failure unless the design specifically takes this challenge into consideration.

Foreign body reactions to wear debris from previous implants may further influence the effectiveness of bioengineered replacements by creating an inflammatory environment detrimental to tissue. Henry and Wolford[53] reported that reconstruction with autogenous materials following Proplast-Teflon implant failure was much less predictable than with total alloplastic TMJ reconstruction. Therefore, patients with particulate wear debris may contraindicate the use of bioengineered tissue devices.

The authors felt that a bioengineered TMJ disc may be indicated to replace unsalvageable articular discs caused by trauma or disease, manage Wilkes Stage III and IV internal derangements, and complement bioengineered condyles in total TMJ replacement cases. Another

potential use may be in the repair of disc perforations, although the urgency for filling perforations is less clear at this time. The utility of bioengineered discs is a point of debate since complete disc removal without disc replacement though controversial has yielded satisfactory long-term results (i.e., pain reduction and improved joint mobility).[41] Also, surgical placement and attachment of the disc to surrounding structures is of the utmost concern.[4] Since the disc must move with opening and closing of the jaw, the device may be prone to failure if it does not possess adequate mechanical integrity to oppose all of the forces associated with ginglymo-diarthroidial articulation. A fossa liner seems to be a more surgically viable approach and can be sutured to the fossa to serve as an interpositional buffer between the eminence and condyle to promote joint congruence while improving mandibular function. Nonetheless, true bioengineered discs may still prove to be an even better option if basic complications relating to attachment, articulation and mechanical integrity can be overcome.

As bioengineers move forward with the translation of engineered tissues, it will be necessary to consider both pre-clinical animal models and clinical trials. Although TMJ tissue engineering strategies have not yet reached the stage of clinical trials, some consideration has been given to animal models. At the first TMJ Bioengineering Conference in 2006, the pig was selected as a preferred animal model for TMJ tissue engineering animal studies,[4] and in fact a porcine model has been employed in a leading TMJ tissue engineering study.[54] However, since that time, anecdotal concerns have been raised with respect to the continued growth of the porcine skeletal structure, and alternate animal models including goats and sheep have been suggested. We consider animal model selection an open question that remains to be resolved, but we have further reviewed these issues elsewhere.[55, 56] In the context of the current paper, we may

even suggest that different animal models may be more well suited to different types of indications.

The proposed indications outlined in this paper are intended to be informative, highlight early thoughts on the clinical need for bioengineered TMJ devices, and develop a basis for a continued dialogue between investigators in this field and clinicians. Investigators are encouraged to address these needs by developing innovative management strategies to improve outcomes for patients with TMJ disorders. This paper is designed to be used as a resource to help justify the significance of TMJ-related bioengineering research, and to guide the field toward yielding clinically useful therapies.

Chapter 3: Development of Chondroinductive Printable Hydrogel

INTRODUCTION

In recent years, three-dimensional (3D) printing has gained significant traction in the field of tissue engineering, enabling researchers to construct complex scaffolds at micrometer-scale resolutions through the controlled deposition of material in sequential layers.[57] The upsurge of free, open-source 3D printing hardware and software as well as on-line file sharing has made it possible to make substantial improvements to commercial desktop 3D printers to facilitate the fabrication of novel scaffolds for tissue-engineering applications.[58] Printing tools can also be created at low-cost to add printing capabilities, such as syringe-based extrusion to enable the 3D assembly of novel viscoelastic inks. For personalized scaffold production, diagnostic imaging and computer-aided design (CAD) modeling can be used to create digital models with patient-specific geometries and custom-designed microarchitectures.[59] In this manner, scaffolds can be designed and manufactured to better mimic the macro- and microscale features of native tissue, which direct cell fate and tissue regeneration.[60] However, 3D-printed scaffolds that meet the biological, chemical and mechanical requirements of native tissue have not yet been realized.[61]

To better recapitulate the complexities of native tissue, 3D-printed hydrogels have been under development to enhance tissue regeneration and overcome the limitations of hydrogels formed by traditional processing techniques, such as mold-casting.[62, 63] Hydrogels, which are hydrated, 3D polymer networks, have shown great promise as scaffolds for tissue engineering due to their aqueous environment, efficient nutrient flux, tunable mechanical properties, and ability to sustain cellular activities and induce tissue-specific differentiation.[61, 64, 65] In particular, hydrogels based on natural polymers, such as alginate, chitosan, hyaluronic acid and gelatin, offer various advantages over synthetic hydrogels and are predominately used in tissue

engineering since they contain biochemical and biophysical stimuli that encourage positive cell-material interactions, which are essential for cell adhesion, proliferation and differentiation.[63, 66] However, the printability and bioactivity of natural hydrogels may vary from batch-to-batch. Variations in material properties make scaffold reproduction challenging and material-induced cell responses unpredictable.[67] In general, natural hydrogels also have limited mechanical robustness compared to hydrogels made with synthetic polymers.[62] Besides these intrinsic disadvantages, it has been widely observed that there is an opposing relationship between the printability of a given hydrogel and its efficacy *in vitro*.[67] Optimal printability and shape maintenance is often achieved with high molecular-weight polymers, degrees of crosslinking and polymer concentrations, whereas cells tend to thrive best when the same properties are dramatically lowered.[67] This inverse relationship drives researchers to select hydrogel properties in the intermediate range to balance cellular activity with shape fidelity. To date, several acellular and cell-laden hydrogel inks have been investigated, but there is still a shortage of printable yet cell-instructive hydrogels.[66] Therefore, advanced hydrogel inks must be developed to overcome these opposing requirements.

Hydrogel printing through syringe-based extrusion operates at ambient conditions and dispenses filamentous strands of viscoelastic ink in a layer-by-layer fashion.[68] For successful printing, hydrogel inks must flow and not obstruct the extrusion tool, and must be rapidly stabilized once deposited to maintain the shape and structure of the deposited layer so that successive layers can be printed on top without detrimental effects.[68] Hydrogel printing resolution and cell survival, proliferation and differentiation are reliant on many factors and their interactions including: polymer concentration, molecular weight, gelation mechanism, mechanical properties, crosslinking density, rheological properties, print head positioning and

extrusion accuracies, and printing parameters.[67] High-viscosity, shear-thinning inks with observable yield stresses are ideal so that the material flows more easily through the dispensing tip where it is exposed to high shear stresses, and is prevented from flowing when low or negligible shear stresses are applied.[67] High viscosities and yield stresses also serve to prevent filament collapse once deposited. However, even the most viscous inks will still experience flattening and losses in shape fidelity over time. Therefore, it is of great benefit for the printed hydrogel ink layers to be quickly stabilized through post-deposition crosslinking to achieve long-term structural integrity.

Hyaluronic acid (HA) is a non-sulfated glycosaminoglycan, is an essential component of articular cartilage, and can be functionalized to form photocrosslinkable hydrogel ink. Furthermore, to improve cartilage regeneration therapies, there is a growing interest in the incorporation of extracellular matrix (ECM) derived from articular cartilage into scaffolds to better replicate the native cellular environment since the matrix contains cartilage-specific growth factors and epitopes. Cartilage ECM-based scaffolds have been shown to promote cartilage-specific differentiation in the absence of exogenous growth factors, and several studies have also reported enhanced cartilage repair *in vivo*.[69-71] To prevent adverse immune response in the host, native tissues must go through a process called decellularization to remove cellular components and associated epitopes that elicit foreign body reactions. Our group has previously demonstrated that micron-sized decellularized cartilage (DCC) enhanced methacrylated hyaluronic acid (MeHA) hydrogel for direct injection into focal cartilage defects to initiate hyaline cartilage regeneration.[72] From previous studies, MeHA/DCC pre-gel was shown to exhibit paste-like rheological properties, and had observable yield stresses that enabled it to be injected into cartilage defects without flowing away.[72] The pre-gel once applied could be spread

into place and photocrosslinked *in situ*. Furthermore, this material was found to guide chondrogenesis.[72]

While injectable MeHA/DCC pre-gel is useful for focal defect repair, an injectable hydrogel treatment would not be appropriate for the repair of large-sized defects with complex structures. 3D-printed hydrogels customized to exact patient specifications would be more suitable for large defect repair or joint resurfacing, and would better reproduce the anatomical structure of the articular cartilage unique to each patient. Though MeHA/DCC pre-gel possesses rheological properties that are favorable for 3D printing, it has a curing time of approximately 15 minutes, making it impractical for multilayered 3D construction, which demands rapid crosslinking. Therefore, different crosslinking chemistry was employed in the current study to improve gelation time in order to quickly stabilize printed hydrogel layers and decrease printing times. Pentenoate groups were attached to the HA backbone to facilitate photocrosslinking through thiol-ene 'click' chemistry (Figure 3.1). These 'click' reactions are highly efficient and reduce the gelation time to 2.8 min, making pentenoate-modified HA (PHA) a more viable alternative to MeHA for 3D printing.[73]

The objective of the study was therefore to design and optimize hydrogel ink comprised of PHA and DCC microparticles for extrusion-based printing, and test the efficacy of the crosslinked hydrogels for cartilage regeneration. To establish hydrogel printing capabilities, open-source hardware and software were used to build a syringe-based extrusion tool, which was connected to an FDM 3D printer. Next, studies were performed to evaluate the printability and associated rheological properties of PHA hydrogels with various polymer molecular weights, polymer contents and concentrations of DCC microparticles. The mechanical properties and swelling behavior of the hydrogels were also evaluated to determine the robustness and

equilibrium swelling behavior of the hydrogels. Lastly, the efficacy of PHA/DCC hydrogel for articular cartilage regeneration was investigated *in vitro* by evaluating cellular adhesion, proliferation, chondrogenic gene expression, and through microscopic visualization of the neotissue using histological staining.

MATERIALS AND METHODS

Materials Synthesis

Pentenoate-Modified Hyaluronic Acid

To synthesize hyaluronic acid capable of photo-polymerization, hyaluronic acid was functionalized with pentenoate groups through the esterification of free hydroxyl groups on the polymer backbone with pentenoic anhydride as described by Mergy *et al.*[73] (Figure 3.1A). Briefly, 1 w/v% sodium hyaluronate (1 MDa, Lifecore Biomedical, MN) was solubilized in deionized water and mixed with dimethylformamide (DMF) to achieve a DMF/water v/v ratio of 2:3. Under continuous stirring, 4-pentenoic anhydride (Sigma-Aldrich, MO) was added in 5-fold molar excess to sodium hyaluronate, and the pH of the mixture was maintained between 8 and 9 through periodic additions of 0.5M NaOH. Once the pH ceased to change (about 6 hours), sodium chloride (NaCl) was added to achieve a 0.5M NaCl solution. The product was precipitated in acetone, which was added to the reaction mixture to obtain an acetone/water v/v ratio of 5:1. The precipitate was collected by centrifugation at 7800 rpm and subsequently dissolved in deionized water, loaded into dialysis tubing (3500 Da molecular weight cut-off) and dialyzed against deionized water for 48 hours. The purified PHA was then freeze-dried and stored at -20°C. The purity and degree of functionalization was determined through ^{1}H NMR spectroscopy.

Micron-Sized Decellularized Cartilage

Ten porcine knee joints from male Berkshire hogs were obtained from Bichelmeyer Meats (Kansas City, KS) and articular cartilage from the pattelofemoral and tibiofemoral surfaces was shaved off with a scalpel. Cartilage shavings were rinsed with deionized water and stored at -20°C until further processing. Prior to decellularization, the cartilage shavings were fragmented into coarse granules to decrease the diffusion distance required for decellularization agents to reach inhabiting cells, and was performed using a high-speed blade mill (CryogenicTissueGrinder, Bio Spec Products, Bartlesville, OK) in the presence of dry ice. After fragmentation, the coarse-ground cartilage was stored overnight at -20°C to allow for dry ice sublimation. To test the efficiency of the decellularization process, a portion of coarse-ground cartilage was retained for further analysis (i.e., fluorometric double-stranded (ds) DNA quantitation). Decellularization was carried out following the protocol described in Sutherland *et al*.,[69] which involves the successive immersion and agitation of coarse-ground cartilage in various decellularization agents including: hypertonic solutions, ionic and nonionic detergents, enzymatic nuclease solution and ion exchange resin suspensions.

To summarize, coarse-ground cartilage was packaged into pre-soaked dialysis tubing (3500 Da molecular weight cut-off), sealed with clamps and placed in wide-mouth jars containing hypertonic saline solution to induce cell shrinkage and detachment from surrounding extracellular matrix.[74] The jars were placed in a shaking incubator and were maintained at 200 rpm for 24 hours. Unless otherwise noted, each immersion step in the decellularization process was subjected to agitation at a speed of 200 rpm. The packaged cartilage was then placed in 0.05 v/v% Triton X-100, a nonionic detergent, for 3 hours to solubilize and remove proteins.[74] Next,

the tissue was exposed to 0.0625 KU/mL benzonase nuclease for 12 hours to cleave nucleotide chains through enzyme action, and was followed by two one-hour immersions in deionized water. The packaged cartilage was then placed in 1 v/v% n-lauroyl sarcosine, an anionic detergent, for 12 hours at 21°C and 70 rpm to further solubilize cellular materials. Following treatment with n-lauroyl sarcosine, the tissue was immersed in 40% ethanol for 30 minutes, and placed in a suspension containing three types of organic ion exchange resins to extract organic compounds and remove residual cellular components for 12 hours.[74] The packaged cartilage was then transferred into a hypertonic saline solution at 21°C and 70 rpm for 2 hours. After decellularization, the cartilage-derived ECM remaining in the dialysis tubing was removed and freeze-dried. Once dehydrated, the coarse-ground decellularized cartilage was pulverized using a cryogenic mill (6775 Freezer/Mill, SPEX SamplePrep, Metuchen, NJ). The resulting DCC powder was filtered to ensure that particles in at least one dimension did not exceed 45 μm and was stored at -20°C.[69]

To assess the extent of decellularization, dsDNA concentrations of coarse-ground native cartilage and DCC microparticles were quantitated using a Quant-iT™ PicoGreen® dsDNA Assay Kit (ThermoFisher Scientific) and fluorescence plate reader. To prepare samples for testing, coarse-ground cartilage and DCC microparticles samples (n=3) were carefully weighed and digested in solution containing 4.5 μL/mL papain, 2.8 mg/mL EDTA, 1.8 mg/mL n-acetyl cysteine, 2.7 mg/mL potassium phosphate monobasic and 13.7 mg/mL potassium phosphate dibasic in distilled water. Next, the samples were vortexed to break up clumps and kept overnight at 60°C to achieve complete digestion. Following the recommended assay protocol, 10 μL of each digested sample and 90 μL of 1X TE Buffer (20-fold dilution of 10 mM Tris-HCl and 1 mM EDTA) were transferred into wells of a black 96-well plate in triplicate. 100 μL of 200-

fold Quant-iT™ PicoGreen® reagent was pipetted into each well and was incubated for 5 minutes at room temperature in dark conditions. After incubation, the fluorescence (480 nm excitation and 520 nm emission wavelengths) was measured with a plate reader. In parallel, lambda dsDNA standard dilutions ranging from 10 ng/mL to 1 μg/mL dsDNA were prepared in 1X TE Buffer to generate a 6-point standard curve. The fluorescence of each dilution was measured after incubation with the Quant-iT™ PicoGreen® reagent and a linear regression model was fit to the data.

Hydrogel Precursor Preparation

To prepare the radical photoinitiator solution, 5 mg of IRGACURE 2959 (1-[4-(2-Hydroxyethyoxy)-phenyl]-2-hydroxy-2-methyl-1-propane-1-one, Ciba Specialty Chemicals) was mixed with 10 mL of sterile PBS (0.05 w/v% IRGACURE 2959) and heated to 60°C to dissolve. To yield 10 mL of UV-crosslinkable hydrogel precursor, 300 mg of PHA, an equimolar amount (116.87 mg) of dithiothreitol (DTT), and various amounts of DCC (0, 500, 1000 and 1500 mg) were combined with 10 mL of 0.05 w/v% IRGACURE 2959 solution to achieve prescribed PHA and DCC concentrations of 3 w/v% and 0, 5, 10 and 15 w/v%, respectively. After an even consistency was obtained through vigorous stirring, the hydrogel precursor mixtures were centrifuged to remove bubbles, and were protected from light until further use.[73]

Hydrogel Printing

3D Printer and Custom Modifications

An FDM machine (RepRapPro Tricolour Mendel 3D Printer) that supports three motor-driven Bowden extruders was purchased from RepRap Professional Limited (Bristol, UK), and

was assembled according to the manufacturer's instructions. To expand the printer's capabilities and enable viscoelastic ink deposition through syringe-based extrusion, a 3D-printed syringe pump was fabricated and connected to the controller board in place of one of the three filament extruders. The main component parts for the linear actuator were printed with polylactic acid (PLA, 1.75mm MakerBot PLA filament), and the metal fasteners were purchased from Amazon.com and McMaster-Carr (the complete bill of materials can be found on-line at http://www.appropedia.org/open-source_syringe_pump). The STL files for the linear actuator parts were designed by Michigan Tech's Open Sustainability and Technology Lab and were downloaded from a GitHub repository (https://github.com/mtu-most/linear-actuator).[75] A modified plunger holder designed by Dylan Lynch was printed to enable front-loading of 10-mL syringes onto the linear actuator. The STL file of this component was retrieved from Thingiverse (http://www.thingiverse.com/thing:578010). Once assembled, the linear actuator was attached to a NEMA stepper motor and connected to the Melzi 2.0 slave controller board. The motor steps per mm value was determined through calibration tests and defined in the Marlin firmware. A 3D-printed mount for the dispensing tip was designed and secured to the motor-controlled printer carriage. The syringe pump was suspended above the print bed and tubing and Luer-Lok connectors were used to attach the syringe tip to the dispensing tip (Figure 3.2). Lastly, a UV lamp (312 nm) was positioned over the print bed to induce the gelation of photocrosslinkable extrudates.

Printability Tests and Print Quality Refinement

The printability of PHA hydrogel precursor solutions with various polymer contents (2, 3 and 4 PHA w/v%) and molecular weights (100, 500, 700 and 1000 kDa) was examined through

extrusion and single-layer print tests using the syringe-based extrusion tool. First, to perform extrusion tests, PHA pre-gels were loaded into syringes, coupled to the extrusion tool, and driven through the associated tubing and 20-gauge dispensing tip through direct command of the stepper motor using Pronterface (host interface) software and the quality of the extrudates were assessed. Next, single-layer print tests were performed to evaluate the ability of PHA pre-gels to deposit onto the surface of the build plate in continuous filaments and to determine the influence of polymer concentration and molecular weight on the shape fidelity and spatial resolution of the printed pre-gels.

Based on the printability tests, 3 w/v% 1 MDa-PHA pre-gel, which yielded the highest-resolution single-layer test prints, was selected to investigate the effect of DCC microparticles on the printability of the PHA pre-gel. In addition to extrusion and single-layer print tests, multilayered print tests were performed to develop a method for printing 3D objects and to obtain baseline parameters for printing with 3 w/v% PHA pre-gels containing various concentrations of DCC microparticles (0, 5, 10, 15 and 20 w/v%) using the syringe-based extrusion tool. Parametric studies were performed to refine the quality of 16-layer 1 cm x 1 cm printed hydrogels by adjusting the following parameters in the slicing software: plotting speed, plotting volume, retraction length and speed, size and shape of dispensing tip, UV curing time, extrusion width and height among others. In addition, certain manual adjustments were made to the software-generated G-code script to further optimize the hydrogel printing process. The hardware, software, firmware and slicing settings were all manipulated in tandem to manufacture 3D-printed hydrogels of satisfactory quality.

Hydrogel Cast-Molding

Mold-casted hydrogel groups were made by transferring PHA/DCC pre-gel into a rectangular silicone gasket affixed to a glass slide. A second glass slide was used to press-fit the mixture into the mold and form a seal with the gasket to create a pre-polymerized slab with a defined thickness of 2.25 mm. The slab was irradiated with UV light (312 nm) for 4 minutes on each side to allow for uniform crosslinking, and a 4-mm biopsy punch was used to create cylindrical samples for further characterization.

Rheological Evaluation of Hydrogel Precursors

To evaluate the influence of DCC concentration on the rheological behavior of hydrogel precursor mixtures, steady state flow and oscillation tests were performed with an AR 2000 Rheometer (TA Instruments, New Castle, DE) on PHA pre-gels with 0, 5, 10 and 15% DCC microparticles. All tests were performed at 25°C to mimic printing conditions using a 20-mm crosshatched Peltier plate geometry with a solvent trap and cover to retain hydration and prevent light exposure. A truncation gap of 500 μm was used for all the tests. To create flow curves (viscosity-shear rate profiles), shear rate sweeps from 0.001 to 1000 1/s were applied to samples and viscosity was recorded once steady state was achieved. Next, oscillatory stress sweeps were performed from 1 to 500 Pa at 1 Hz to determine the storage and loss moduli in the linear viscoelastic (LVE) region (i.e., stress- and strain-independent region) and the magnitude of observable yield stresses. Initial frequency sweeps were also conducted to validate that the viscoelastic behavior of pre-gels at 1 Hz was linear.

Mechanical Characterization

Uniaxial, unconfined compression tests were performed to determine the compressive modulus and strength of PHA/DCC hydrogel groups (n=6) using an RSA III Dynamic Mechanical Analyzer (DMA, TA Instruments, New Castle, DE). PHA hydrogels enhanced with 0, 5, 10 and 15 w/v% DCC microparticles were fabricated by 3D printing and mold-casting methods to study the effects of both DCC concentration and fabrication method on hydrogel stiffness and strength. To fabricate 3D-printed samples for testing, 12-layered hydrogel slabs were printed as described above with layer heights of 0.17 – 0.25 mm (contingent on hydrogel formulation) corresponding to overall heights of 2-3 mm. Cylindrical samples were punched out of 3D-printed and mold-casted hydrogel slabs with a 4-mm biopsy punch, and were submerged in PBS for 24 hours to establish equilibrium swelling. Preceding testing, swollen hydrogels were blot-dried, and their mean diameters were measured using digital calipers under 20X magnification, and their heights were measured with the DMA. A strain rate of 0.005 mm/s was applied to samples until mechanical failure was reached. The slope of the elastic region of the stress-strain curve (i.e., 0-10% strain) was calculated as the compressive modulus, and the ultimate compressive strength of each sample was taken to be the stress at the point of permanent yield (i.e., fracture point).

Swelling Degree

To determine the swelling ratio of PHA/DCC hydrogel formulations, cylindrical samples were punched out of mold-casted hydrogel slabs using a 4-mm biopsy punch. The samples were submerged in PBS for 24 hours to establish swelling equilibrium and were carefully weighed after blotting to remove excess solution. Each sample was then freeze-dried and their weights

were again measured. The swelling ratio (S) of each sample group was determined using the equation:

$S = [(W_H - W_D)/W_D]$,

where W_H is the weight of the fully hydrated gel and W_D is the weight of the dehydrated gel. Each swelling ratio is reported as the average of six samples.

Cell Harvest and Culture

Rat bone marrow-derived mesenchymal stem cells (rBMSCs) were harvested from male Spraque Dawley rats in strict accordance with an IACUC-approved protocol at the University of Kansas. Bone marrow was flushed from the femur bones with sterile PBS containing 1 v/v% antibiotic-antimycoctic (anti-anti) and plated in tissue culture flasks containing Minimum Essential Medium Eagle Alpha Modification (α-MEM) supplemented with 10 v/v% qualified fetal bovine serum (FBS) and 1 v/v% anti-anti. Culture medium was replenished every 2-3 days and the cells were subcultured after approximately 80% confluent. Following the first subculture, cells were maintained in α-MEM containing 10 v/v% FBS and 1 v/v% penicillin-streptomycin (pen-strep) and underwent expansion until passage 4. Unless otherwise stated, all cell culture supplies were purchased from Thermo Fisher Scientific.

Hydrogel Disc Preparation and Cell Seeding

Hydrogel discs were created for insertion into multi-well plates for 2D *in vitro* studies to assess the viability, proliferation and differentiation of seeded rBMSCs. First, all dry materials were sterilized with ethylene oxide (Anprolene AN74i Gas Sterilizer, Andersen Products, Haw River, NC), and all wet materials were sterilized in an autoclave or with Steriflip® filter units.

To prepare hydrogel discs, a small volume of hydrogel precursor mixture was deposited into a petri dish and was flattened to a height of 150 μm with a glass slide using spacers. The petri dish containing the pre-polymerized disc was then placed under UV light for 4 minutes to achieve complete gelation. To aid in the detachment of the polymerized discs, PBS was added to the petri dishes before retrieval. The crosslinked discs were washed twice with PBS and were then soaked overnight in PBS containing 1 v/v% pen-strep. Prior to cell seeding, the discs were plated into multi-well plates and placed under the germicidal UV lamp in the laminar flow hood for 30 minutes for further disinfection. rBMSCs at passage 4 were trypsinized, resuspended in fresh culture media, counted using an automated cell counter (Cellometer, Nexcelom Bioscience) and pipetted onto the hydrogel discs for all *in vitro* experiments. Unless otherwise stated, cell cultures were maintained in α-MEM containing 10 v/v% FBS and 1 v/v% pen-strep, which was replenished every other day.

Cell Viability

A LIVE/DEAD Viability/Cytotoxicity Kit for mammalian cells (Molecular Probes, Eugene, OR) was used to visualize the viability of rBMSCs cultured on PHA/DCC hydrogels. Hydrogel discs (d=22 mm, h=150 μm) were fabricated as described above, plated in 12-well plates, and seeded with rBMSCs (100,000 cells/well, passage number 5, n=5). After 24 hours, 3 days and 10 days of 2D culture, samples were labeled with fluorescent markers to visualize and distinguish live- and dead-cell populations within each well. Initially, culture medium was removed from the wells and the samples were washed twice with PBS to remove serum and reduce the background signal. Next, 300 μL of 0.5 μM calcein AM and 2 μM ethidium homodimer-1 in PBS was distributed to each well, incubated for 15 minutes at 37°C and 5%

CO_2, and protected from light. The samples were again washed with PBS and subsequently imaged with a fluorescence microscope (Axio Observer A1 Inverted Microscope and AxioCam MRm Fluorescence Camera, ZEISS). The live-cell population was labeled with green-fluorescent dye and the dead-cell population was labeled with red-fluorescent dye.

Cell Proliferation

To measure the relative number of viable cells on hydrogels at 1, 3 and 10 days a colormetric proliferation assay (CellTiter 96 AQ_{ueous} One Solution Cell Proliferation Assay, Promega, Madison, WI) was performed. PHA/DCC hydrogel discs with diameters of 11 mm and heights of 150 μm were prepared as described above, inserted into 48-well plates, and seeded with rBMSCs at a density of 40,000 cells/well. Prior to performing the assay, culture media was removed and 200 μL of fresh media was added to each well. After 1 hour of incubation in fresh media, 20 μL of CellTiter 96 AQ_{ueous} One Solution Reagent (containing MTS and PES) was transferred to each well and the plate was incubated at 37°C and 5% CO_2 for 3 hours. After incubation, 150 μL of solution from each well was transferred to a 96-well plate and the absorbance at 490 nm was read using a plate reader. To obtain the relative cellular metabolic activities, absorbance values for each gel formulation were normalized to the mean of the corresponding group at day 1.

Cell Differentiation Evaluation

To determine the potential efficacy of PHA/DCC hydrogel for *in situ* cartilage regeneration, a 4-week *in vitro* study was conducted to 1) evaluate the expression of chondrogenic and osteogenic genes in seeded rBMSCs through quantitative reverse transcriptase

polymerase chain reaction (RT-qPCR) methods and 2) visualize cell organization and cartilage-specific tissue deposition using histological techniques. PHA/DCC hydrogel discs containing 5, 10 and 15 w/v% DCC were tested to evaluate the effect of DCC concentration on the type and quality of tissue synthesized by rBMSCs. PHA hydrogel without DCC was used as a negative control and PHA hydrogel cultured in chondroinductive media containing transforming growth factor-beta 3 (TGF-ß3) was used as a positive control. The chondroinductive media used throughout the study consisted of α-MEM with 10 ng/mL TGF-ß3 (human recombinant, PeproTech), 50 µg/mL ascorbic acid, 1 v/v% pen-strep, 40 µg/mL l-proline, 100 µM sodium pyruvate, 0.1 µM dexamethasone (MP Biomedicals), 1 v/v% insulin-transferrin-selenium and 1% non-essential amino acids, and is known to be a potent inducer of chondrogenesis and hyaline-like cartilage formation in progenitor cells.[76] Hydrogel discs (d=15.5 mm, h=150 µm) were fabricated to fit into 24-well plates and all wells were seeded with 40,000 rBMSCs.

Relative Gene Expression Quantitation

RT-qPCR was performed to investigate the relative expression levels or fold changes in the expression of chondro- and osteogenic genes in rBMSCs cultured on PHA/DCC hydrogel discs (n=6) at prescribed time points of 1, 14 and 28 days. First, media was removed from the well plates and samples were washed twice with PBS. Following an established protocol, mRNA was purified from the rBMSCs using an RNeasy Mini Kit (Qiagen, Hilden, Germany). To measure the concentration and purity of the isolated mRNA, a NanoDrop 2000 Spectrophotometer (Thermo Fisher Scientific) was used. mRNA samples with absorbance ratios (A_{260}/A_{280}) within the range of 1.8-2.2 were considered to be of acceptable purity and were reverse-transcribed to complementary DNA (cDNA). Reverse transcription (RT) reactions were

carried out using a High Capacity cDNA Reverse Transcription Kit (Applied Biosystems, Foster City, CA) in a thermal cycler (Eppendorf Mastercycler ep Gradient S). TaqMan® Gene Expression Assays and TaqMan® Fast Universal PCR Master Mix (2x), No AmpErase UNG (Applied Biosystems, Thermo Fisher Scientific) were used to amplify the cDNA templates and detect the following genes of interest: glyceraldehyde phosphate dehydrogenase (GAPDH, Assay ID: Rn01775763_g1), sex-determining region-Y-box 9 (SOX9, Assay ID: Rn01751070_mH), collagen type II alpha-1 chain (COL2A1, Assay ID: Rn01637087_m1), aggrecan (ACAN, Assay ID: Rn00573424_m1), and collagen type I alpha-1 chain (COL1A1, Assay ID: Rn01463848_m1). The assays were run in a thermal cycler using 'Fast' thermal cycling conditions, and the expression levels of target genes were normalized to GAPDH, the endogenous control. Each sample was assessed in duplicate. The comparative C_T method was used to quantitate the expression levels of target genes normalized to the endogenous control and relative to the negative control group at day 1, also known as the reference sample. Results are reported as fold changes in gene expression from the negative control group at day 1.

Histological Examination

Histological staining was used to resolve the spatial organization and ECM deposition of rBMSCs on PHA/DCC hydrogels *in vitro*. At 1, 14 and 28 days, culture media was removed from the wells and samples were fixed in 10% neutral buffered formalin overnight at 4°C. After the fixative was discarded, the wells were washed twice with PBS. To visualize the morphology and distribution pattern of cells, hematoxylin and eosin (H&E) solutions were used to stain nuclei and cellular cytoplasm, respectively. Briefly, samples were exposed to Hematoxylin QS (H-3404, Vector Laboratories, Burlingame, CA) for 5 minutes and then washed with 1 v/v% HCl

in 70 v/v% ethanol. Next, samples were exposed to bluing reagent (Richard-Allan Scientific Signature Series Bluing Reagent, Thermo Fisher Scientific) for 5 minutes, washed with deionized water, and exposed to 0.25 w/v% eosin for 20 seconds. The wells were washed twice with deionized water, and incubated in PBS at 4°C for one week prior to imaging to reduce the intensity of the stain. Additionally, Safranin-O and Fast Green dyes were used to stain proteoglycans red and non-collagen sites green for contrast. Initially, formalin-fixed samples were immersed in a 1:10 dilution of Hematoxylin QS for 4 minutes and washed with deionized water. Next, 0.04 w/v% Fast Green was applied to each sample for 4 minutes, 0.1 v/v% acetic acid was applied for 30 seconds, and 0.05 w/v% Safranin-O was applied for 4 minutes. Samples were washed with deionized water and imaged after soaking in PBS for one week. To further visualize cell distribution and organization, fluorescence microscopy was performed, and Alexa Fluor® 488 Phalloidin and DAPI (4',6-Diamidino-2-Phenylindole, Dilactate) dyes were used to label F-actin and cell nuclei, respectively. First, formalin-fixed samples were washed twice with PBS and immersed in 0.1% Triton X-100 (IBI Scientific) in PBS for 20 minutes. After two washes with PBS and in dark conditions, phalloidin dye was diluted in 0.1% BSA (1:40 dilution) and was added to wells for 45 minutes. Samples were washed twice with PBS and then soaked in DAPI dilactate in PBS (1:100 dilution) for 5 minutes. Samples were washed with PBS and immediately imaged under both UV and blue excitation. All images were acquired with a ZEISS Axio Observer A1 inverted microscope equipped with ZEISS AxioCam color and fluorescence cameras.

Statistical Analysis

Statistical analyses were carried out with R statistical software. For single-factor experiments (e.g., hydrogel formulation), one-way analysis of variance (ANOVA) was used to determine whether statistically significant differences were present between mean treatment effects. For two-factorial experiments (e.g., hydrogel formulation and fabrication method), two-way ANOVAs were conducted to test omnibus hypotheses. For pairwise comparisons, simultaneous Tukey's Honestly Significant Differences (HSD) post-hoc tests were performed with 95% family-wise confidence levels. Observed differences among treatment effects were considered statistically significant when their calculated p-value was less than 0.05. To infer statistical significance ($p < 0.05$) for RT-qPCR experiments, the pre-transformed threshold cycle normalized to the internal control gene and negative control group ($\Delta\Delta Ct$) was selected as the response variable in the two-way ANOVA models and subsequent Tukey's HSD tests for each gene of interest. Quantitative results are presented as the mean value ± standard deviation.

RESULTS AND DISCUSSION

Material Characterization

HA was chemically modified with alkene functionalities to enable hydrogel formation through photocrosslinking. To this end, pentenoate groups were grafted onto the HA backbone through esterification of the primary hydroxyl groups. ^{H}NMR spectroscopy was performed to confirm successful derivatization of HA and to determine the degree of functionalization (DF). The resonance signals at around 2.25, 2.5, 5.0 and 7.5 ppm are indicative of HA derivatization and correspond to the hydrogen atoms located along the chain of the pentenoate group (Figure 3.3). To calculate the DF, peaks located at around 5.75 ppm and 1.75 ppm of the NMR spectra

were integrated, corresponding to hydrogen atoms located on the pentenoate double bond (labeled HC) and hydrogen atoms located on the acetyl group of the HA molecule (labeled H2''), respectively. The integrated intensities were compared to obtain the ratio of pentenoate groups to hyaluronic acid molecules. The DF from the representative spectra shown in Figure 3.3 was determined to be 22% pentenoate groups per HA molecule, and the DF for all batches of PHA used in the current study ranged from 22-28%. After chemical modification, PHA was reacted with a dithiol compound (DTT) in photoinitiator (Irgacure 2959) solution to form thioether bridges between pendant pentenoate groups to form a stable crosslinked network through photoinduction. Based on observation, PHA pre-gels underwent complete gelation within approximately 3 minutes of UV exposure, echoing the findings of Mergy *et al*.[73] The crosslinking density of the hydrogel is limited by the DF of PHA, which is modulated by the molar ratio of pentenoate anhydride to hyaluronic acid in the esterification reaction. Though DF was not varied in the current study, crosslinking density has been shown to have opposing effects on the printability and tissue-forming capacity of hydrogels.[67, 77] Since the mesh size or effective porosity of the hydrogel network is decreased when the degree of crosslinking is increased, the diffusion rate of nutrients is lower and tissue ingrowth is more obstructed at higher crosslinking densities.[77] In contrast, the mechanical stability and therefore printability of the hydrogel is enhanced when highly crosslinked. Therefore, the crosslinking density of PHA hydrogel should be optimized in the future to balance these antagonistic effects.

The objective of decellularization was to create cartilage-derived particles that were both chondroinductive and immunoneutral for incorporation into PHA hydrogels. Toward this objective, porcine cartilage was decellularized to remove cellular components and associated epitopes to reduce the risk of inflammatory or adverse immune responses, while retaining the

physicochemical characteristics of the ECM to preserve bioactive cues, which have been shown to potentiate chondrogenic differentiation of progenitor cells.[69] Through the use of specific enzymes, detergents, osmotic shock, and physical fragmentation, the dsDNA content was reduced in porcine-derived articular cartilage as quantified through Quant-iT PicoGreen assays (Figure 3.4). Cryoground native cartilage contained 1023 ± 31 ng dsDNA per mg dry material and cryoground DCC contained 242 ± 26 ng dsDNA per mg dry material. The efficiency of the method, defined as the percent decrease of dsDNA content in cryoground cartilage pre- and post-decellularization, was determined to be 76.4%. Currently, there are no standardized or evidence-based guidelines in place to define the decellularization endpoint, nonetheless by convention, tissues with less than 50 ng dsDNA per mg dry material are regarded as decellularized.[74] Though a significant decrease in dsDNA was observed in the DCC, the decellularization method did not reduce dsDNA to this conventional threshold value, and therefore decellularization was considered mild. Though not substantiated in the present study, Sutherland *et al.*[69] observed GAG and collagen retention using an identical decellularization protocol.

Since the tissue derivatives are xenogeneic, cellular remnants may contain the alpha-Gal epitope, which has caused immune-regulated rejection of porcine implants in primates.[78, 79] However, Daly *et al.*[79] found that decellularized tissue did not elicit adverse immune responses in the host even though antibody levels for the alpha-Gal epitope were elevated. Therefore, modifications to the decellularization protocol should be investigated to effectively and reproducibly 1) reduce dsDNA content to acceptable levels (i.e., <50 ng dsDNA per mg of dry material) to prevent immunogenicity in the recipient, and 2) retain biochemical and structural cues to promote cartilage growth.

Hydrogel Printing

PHA hydrogel precursor solutions with various polymer contents (2, 3 and 4 w/v%) and molecular weights (100, 500, 700 and 1000 kDa) were prepared, loaded into syringes, and extruded through the custom-built syringe-based extrusion tool. All 2 and 3 w/v% PHA pre-gels as well as 4 w/v% 100 kDa-PHA pre-gel were capable of motor-driven extrusion through the dispensing tip. In contrast, 4 w/v% pre-gels prepared with 500, 700 and 1000 kDa PHA caused the extrusion tool to jam, and the motor was incapable of driving these pre-gels through the associated tubing and dispensing tip. Though extrudable, the 4 w/v% 100 kDa-PHA pre-gel was nonuniformly dispensed, and caused sporadic blockages in the dispensing tip, resulting in unpredictable sputters. All 4 w/v% PHA pre-gels were difficult to prepare at room temperature, and homogenous solutions could not be fully achieved, which may indicate that the solubility limits of PHA in PBS were reached or exceeded. Therefore, 4 w/v% PHA pre-gels were considered unsuitable for printing.

The consistency of the extrudates was found to be dependent on both PHA molecular weight and content of the pre-gel. 2 and 3 w/v% 100 kDa-PHA pre-gels extruded out of the dispensing tip in fluid-like drops. 2 and 3 w/v% 500 kDa-PHA as well as 2 w/v% 700 kDa-PHA pre-gel formulations extruded as viscous globules, and 3 w/v% 700 kDa-PHA, and 2 and 3 w/v% 1000 kDa-PHA pre-gel formulations were extruded as continuous filaments. An image of the extrusion of 3 w/v% 1000 kDa-PHA pre-gel as a stable, continuous filament is shown in Figure 3.5A.

With the exception of 4 w/v% PHA pre-gels, single-layer print tests were performed to test the printing capabilities of all formulations, in which a series of connected parallel lines were deposited with homogenous filament spacings of 0.2 mm (Figure 3.5C). Not including the 3

w/v% 700 and 1000 kDa-PHA pre-gels, all tested pre-gel formulations were deposited onto the print bed in an irregular fashion. For example, 2 and 3 w/v% 100 kDa-PHA pre-gels had no shape fidelity once deposited, and the extrudates immediately coalesced into droplets, resulting in amorphous prints bearing no resemblance to the CAD model. The print quality improved as both molecular weight and polymer concentration was increased. Accordingly, 3 w/v% 1000 kDa-PHA pre-gel generated the highest-resolution prints, containing deposited filaments that possessed structural integrity and exhibited minimal expansion and flattening. Results from these preliminary printability tests are summarized in Figure 3.5B, in which each formulation is classified as 'unextrudable', 'irregular' or 'printable'. In addition, representative images of printable and irregular hydrogel deposits are shown in Figure 3.5C.

Due to exhibiting the highest observable print quality, 3 w/v% 1000 kDa-PHA pre-gel was selected to investigate the influence of DCC microparticles on the rheological properties and printability of PHA pre-gel. The printing capability of PHA pre-gels with 5, 10, 15 and 20 w/v% DCC particles was investigated. All pre-gel formulations, apart from the 20 w/v% DCC group were considered printable, as they could be deposited in filamentous strands to form defined structures in a layer-by-layer fashion. The 20 w/v% DCC group however was too viscous for motor-driven extrusion and could not be forced out of the syringe and into the associated tubing. The CAD model and corresponding printer tool path for the multilayered print tests are shown in Figure 3.6A, and the gross morphology of the fully realized 16-layered, 3D-printed 1 cm x 1 cm hydrogel structures with 0, 5, 10 and 15 w/v% DCC microparticles can be viewed in Figure 3.6B. All hydrogel structures agreed with the dimensions of the model as measured by digital calipers, and model equivalence was shown to depend on the positioning accuracy of the printer, the exactness of the mechanical calibrations, printing parameter refinement, and the rheological

properties of the material. Filament spacing was adjusted to generate hydrogel structures with no void spaces to resemble articular cartilage for joint resurfacing applications. The print quality of the hydrogel structures was optimized by manipulating the following printing parameters in the slicing software: plotting speed, plotting volume, extrusion width, extrusion height, and various retraction parameters (length, speed, etc.). Additionally, custom G-code was added to the script after every two layers to move the 3D-printed material under the UV light source for 90 seconds to stabilize the structure through photocrosslinking before starting the next two layers.

Though 0, 5, 10 and 15 w/v% DCC groups were printable, all of the 3D-printed rectangular prisms exhibited different appearances and structural qualities. For example, extruded filaments in the 0 w/v% DCC group exhibited higher degrees of filament expansion and flattening as well as interfilament fusion, creating a smoother macroscopic appearance. In contrast, the 15 w/v% DCC group exhibited a higher degree of filament resolution, where the extruded filaments though fused could be distinguished and the structure appeared multilayered in nature. The 5 and 10 w/v% DCC groups exhibited properties that resided somewhere in between, containing both smooth and striated appearances.

Rheological Evaluation

To investigate the viscoelastic behavior and structural properties of the hydrogel precursor mixtures, steady-state flow and oscillation tests were performed. First, steady-state viscosity of pre-gels was measured over a range of shear rates and representative steady-state flow curves are shown in Figure 3.7A. All pre-gel formulations (i.e., 0-15% DCC groups) exhibited shear-thinning behavior, where viscosity was high at low shear rates and decreased with increasing shear rate as the polymer chains disentangled and intermolecular forces were

overcome.[67] For example, the viscosity of the pre-gels at an ultra-low shear rate of 0.001 s^{-1} across all pre-gel groups ranged from 260-1700 Pa-s, but as the shear rate approached 1000 s^{-1}, viscosity measurements among the groups all decreased to ~1 Pa-s. In addition, viscosity measurements taken at low shear rates in the range of 0.001 to 0.01 s^{-1} were higher in magnitude for pre-gels containing higher concentrations of DCC microparticles.

To evaluate the storage modulus (G') and loss modulus (G'') of the material, oscillation tests were performed on the PHA/DCC pre-gels by applying a stress sweep from 1 to 500 Pa. The rheological properties in the linear viscoelastic (LVE) region were determined by averaging the oscillatory measurements of G' and G'' taken at applied shear stresses of 1-10 Pa, and are reported in Figure 3.7C. G' and G'' were shown to increase with increasing DCC concentration, and for the 10 and 15% DCC groups G' was higher than G'' indicating that the elastic properties were dominant at low shear stresses. In addition, the G' and G'' curves for these formulations had crossover points, where the G' and G'' were equivalent. The modulus crossover point is where the viscoelastic behavior of the pre-gel transitions from solid-like to fluid-like. The imposed shear stress at this point, called the yield stress, represents the stress magnitude that must be exceeded to overcome the intermolecular and interparticle forces of the material to induce flow. The 0 and 5% DCC groups did not possess yield stresses as they exhibited fluid-like properties even at low shear stresses (G'' > G'). The yield stresses of the 10 and 15% DCC groups were determined to be 142 ± 18 and 231 ± 51 Pa, respectively (Figure 3.7B).

The rheological properties of printable hydrogel inks are not widely reported in literature, though certain rheological properties have been shown to greatly enhance the printing resolution of viscoelastic materials.[67] Shear-thinning behavior and the presence of a yield stress are two such properties. Shear-thinning behavior is ideal because in the absence of shear stress, the

hydrogel ink possesses high viscosity, but as the shear stress increases, polymer chains disentangle and the material flows more easily. This shear-thinning behavior is an important property so that hydrogel ink can be more easily driven through the extrusion tubing and tip due to apparent decreases in viscosity. Once deposited, shear stress is reduced and the viscosity again increases, providing more resistance to flow, which promotes shape retention. Another property that significantly impacts hydrogel ink printability is yield stress. Materials with yield stresses act as elastic solids when interparticle and intermolecular forces within the hydrogel matrix are stronger than applied stresses. When the applied stress is greater than the yield stress, the structure deforms and begins to flow. Therefore, yield stress enhances the shape fidelity and resolution of printed pre-gels, and prevents drips from the nozzle tip when extrusion is halted, while still allowing material to be dispensed when commanded.

Rheological measurements of the pre-gels were consistent with the printability tests performed in the current study. As previously described, 3D-printed hydrogels manufactured with 0 and 5% DCC groups were more amorphous in nature, as the deposited filaments tended to spread prior to UV curing. The 10 and 15% DCC groups were visibly striated, with stratified layers and visible filament deposition patterns, demonstrating that the presence of a yield stress has an impact on the resolution of the printed structure. Of note, the stepper motor that drives hydrogel extrusion occasionally jammed when printing with 15% DCC pre-gels, which likely represents the maximum allowable viscosity that the printer can extrude. In addition to shear-thinning and the presence of a yield stress, rapid photocrosslinking of deposited PHA/DCC pre-gels enabled immediate structural stabilization of printed layers to enhance resolution and provide a solid foundation for the next layer of the print.

Mechanical Evaluation

To assess the mechanical robustness of 3D-printed PHA/DCC hydrogels, compressive mechanical testing was performed to investigate the effect of DCC concentration as well as the effect of the fabrication method on hydrogel stiffness and strength. The mechanical properties of 3D-printed 3 w/v% PHA hydrogels containing 0, 5, 10 and 15 w/v% DCC particles with no voids were compared to mold-casted equivalents to determine whether 3D printing impacted the mechanical performance of the hydrogels. In fact, since mechanical failure typically occurs at scaffold interfaces, one concern was that the layer-by-layer assembly of 3D-printed hydrogels would reduce the mechanical robustness and therefore viability of the hydrogel to serve as a scaffold for cartilage regeneration. All mechanical testing was performed on hydrogel samples in their equilibrium swelling state to determine the stiffness and strength that they would exhibit in physiological conditions. The compressive modulus or mechanical stiffness, defined as the slope in the elastic region of the stress-strain curve, of 3D-printed gels was found to significantly increase with the addition of DCC particles. 5, 10 and 15% DCC groups had compressive moduli greater than the 0% DCC group ($p < 0.05$), though no statistical differences among DCC-bearing hydrogels could be confirmed (Figure 3.8A). The compressive strength, defined as the stress associated with fracture, of the 3D-printed 15% DCC group was significantly higher than the 3D-printed group without DCC particle suspensions (Figure 3.8B). Specifically, the compressive modulus and strength was highest for the 15% DCC group, which was determined to be 6.8 ± 0.6 kPa, and 70.3 ± 10.4 kPa, respectively. Comparisons of 3D-printed and mold-casted samples revealed that the fabrication method had no significant effect on the mechanical properties of the hydrogels; an important finding that validates 3D printing as a viable alternative to traditional mold casting.

Since cartilage is a load-bearing tissue, the hydrogel must be able to withstand physiological loads and loading patterns. Therefore, hydrogel stiffness, which also regulates stem cell differentiation, must be matched to that of native cartilage to resist physiological loads and provide relevant mechanical cues to promote hyaline-like cartilage production. Native cartilage possesses approximate stiffness values ranging from 240 - 1360 kPa depending on the location, zone and mechanical testing parameters.[80, 81] Since the compressive modulus of PHA/DCC hydrogels are orders of magnitude smaller than that of native articular cartilage, stiffening and strengthening strategies should be explored to improve the mechanical properties. Hydrogel reinforcement strategies such as co-printing internal polymeric cages, and embedding melt-printed lattice structures in mold-casted hydrogels among others have been investigated and have reportedly achieved stiffness values similar to native articular cartilage.[70, 82]

Swelling Behavior

The swelling ratios of pre-swollen to swollen hydrogels after incubation in PBS for 24 hours were calculated for each PHA/DCC hydrogel formulation by measuring the percent increase in the wet sample weight over the dry sample weight. The differences in swelling ratio between hydrogels in their equilibrium swelling state compared to their pre-swollen state were substantial. In particular, the 0, 5, 10 and 15 w/v% DCC groups increased 11.2-, 10.6-, 9.6- and 6.5-fold ($p < 0.05$), respectively after equilibrium solvent absorption. While hydrogel swelling is advantageous to resident cells by increasing the rate of diffusion of nutrients into and cellular waste out of the hydrogel matrix, it is also pertinent to moderate swelling as much as possible insofar as to ensure that 3D-printed hydrogels retain physiologically relevant dimensions to be effective in cartilage tissue engineering applications.[83] The incorporation of DCC particles was

shown to reduce the mass-swelling ratio, and at least in part mitigate increases in volume caused by swelling (Figure 3.9). 10 and 15% DCC groups had lower swelling ratios than 0 and 5% DCC groups ($p < 0.05$), which indicate that the hydrogel microstructure is enhanced by the addition of DCC through increased interparticle forces, which provide resistance to deformation and help restrain the osmotic influx of solvent. Ideally, water content in the hydrogel should resemble that of native cartilage to enable efficient nutrient transport and natural biological processes.[81] The water content in native articular cartilage ranges from 65 w/w% to 80 w/w%, corresponding to respective mass-swelling ratios of 1.86 to 4.[84] Based on swelling behavior alone, the 15% DCC group would be best suited for hydrogel fabrication via 3D printing to minimize the changes in shape and size when placed in hydrated conditions. Still, design strategies would need to account for swelling-associated shape distortion in order to fabricate patient-specific constructs that replicate and regenerate cartilage defects with anatomical precision.

Cell Viability and Proliferation

To demonstrate cell viability, rBMSCs were cultured in 2D for 10 days, and fluorescence-based LIVE/DEAD assays were carried out at predefined intervals to observe live and dead cell populations on the hydrogel discs. Microscopic images are displayed in Figure 3.10A, where live cells are depicted in green and dead cells are depicted in red. The images reveal an abundance of live cells with fibroblastic morphologies, and in comparison very few dead cells were observed. Cell proliferation was observed as evidenced by the sparse distribution of cells at day 1 and full coverage on hydrogel surfaces at day 10. Viability and proliferation seemed to be supported to similar extents by all hydrogel formulations. To quantitatively evaluate the influence of DCC particle concentration on cell proliferation, the metabolic activity

of rBMSCs on each sample was measured by performing MTS proliferation assays at the same time points. As shown in Figure 3.10B, there were no significant increases in cell number from day 1 to day 3 for all hydrogel formulations. There was, however, an increase in cell number in day 10 compared to the prior time points ($p < 0.05$). Respectively, 0, 5, 10 and 15% DCC groups had 26, 39, 50 and 48% increases in relative cell number from day 3 to day 10, though no significant differences were detected in cellular proliferation among hydrogel formulations. Therefore, the addition of DCC microparticles did not affect cellular proliferation with statistical significance.

Cartilage-Specific Gene Expression

SOX9, COL2A1 and ACAN expression levels were quantified through RT-qPCR to evaluate the regulation of these chondrogenic genes in cells cultured on the PHA/DCC hydrogels. COL1A1 levels were also quantified as an indicator for hypertrophy or osteogenic differentiation. The relative expression levels of each chondrogenic and osteogenic gene at each time point are shown in Figure 3.11.

SOX9 expression was upregulated in all groups at weeks 2 and 4 compared to the calibrator control group (i.e., 0% DCC at day 1). In 0% DCC samples, SOX9 expression was 2.2-fold higher in week 2 and 3.5-fold higher in week 4 than on day 1 ($p < 0.05$). SOX9 levels increased by 2.6- and 2.5-fold in 5% DCC samples in weeks 2 and 4, respectively, while 10% DCC samples experienced a transient yet significant decrease in SOX9 expression (11.9% reduction) in week 2 followed by a 3.1-fold increase in week 4 ($p < 0.05$). Notably, 15% DCC samples had higher SOX9 expression levels than all other groups in weeks 2 and 4, levels which increased by 5.5-fold in week 2 and 8.4-fold in week 4 compared to day 1 ($p < 0.05$). There was

a significant decrease in the expression of SOX9 from day 1 to week 2 in the positive control group (i.e., 0% DCC + TGF-ß3) followed by an apparent 3.2-fold increase in week 4. Positive control samples had higher SOX9 expression levels relative to other groups at day 1 by factors of 2.3 to 5.2. COL2A1 expression did not significantly change throughout the study, though the 0% DCC group had significantly higher COL2A1-specific mRNA levels in week 4 compared to week 2 or day 1. Additionally, COL2A1 expression in week 4 was higher in 0% DCC samples than 5, 10 and 15% DCC samples. Likewise, ACAN levels did not significantly change throughout the study, though ACAN levels in the positive control group experienced a transient decrease in week 2. COL1A1 expression levels also remained stable throughout the culture period, with the exception of significant differences between the positive control group and all other groups in week 4, where the positive control group had a relative COL1A1 level of 3.6, and the other groups had relative levels ranging from 0.5 to 1.3.

Overall, the results indicate that DCC enrichment of PHA hydrogel may induce chondrogenesis. The most compelling evidence for DCC-dependent chondrogenesis was that the 15% DCC group had more elevated SOX9 levels than all experimental groups including the positive control group at each time point. SOX9 is required for chondrogenesis and controls transcription of COL2A1 and ACAN among other cartilage-specific matrix proteins by binding to regulatory sequences on introns.[85] Though increases in COL2A1 and ACAN levels were expected, chondrogenesis is a multi-step process, so the rates of transcription of COL2A1 and ACAN genes may have heightened if the culture time was extended and SOX9 expression levels were sustained. Alternatively, the lack of gene upregulation of ECM proteins COL2A1 and ACAN may have been due to the 2D culture conditions. The cells may have overpopulated the

hydrogel surfaces, minimizing their direct contact with the DCC microparticles, which present cell-instructive signals.

The only group that experienced higher COL2A1 expression was the negative control group in week 4, though in general the expression levels remained unchanged. COL1A1, an osteogenic gene, was also tested to ensure that cells were not undergoing hypertrophy or osteogenic differentiation. As expected, COL1A1 expression remained stable. The incorporation of DCC in PHA hydrogel, specifically at a concentration of 15 w/v%, may alone be sufficient to direct differentiation of rBMSCs toward a chondrogenic lineage, since SOX9 levels were higher in 15% DCC samples than in positive control samples, indicating that 15% DCC hydrogels outperformed exogenous TGF-ß3 and dexamethasone supplementation. Though mainly positive, the results herein may be difficult to reproduce due to batch variations in PHA and DCC microparticles. Batch properties are reliant on the degree of pentenoate functionalization, cartilage donor, decellularization efficiency, retention of ECM ligands, and homogeneity of the DCC suspensions in the hydrogels.

Histological Evaluation

Histology was performed to examine hydrogel groups at days 1, 14 and 28 to confirm cartilage-specific tissue formation. H&E staining was performed to visualize cell morphology and distribution. The hematoxylin dye stained cell nuclei deep purple, and the eosin dye was used to counterstain cytoplasm. Figure 3.12 shows the images of H&E staining taken at 20x magnification of all hydrogel groups during the 4-week culture. Cells with fibroblastic morphologies were observed in the 0% DCC and 0% DCC + TGF-ß3 (positive control) groups and visibly multiplied over time. The addition of DCC particles made it difficult to distinguish

nuclei and other cellular structures since it increased hydrogel opacity. Furthermore, background staining of the hydrogel was observed making it all the more difficult to discern structures of interest.

Safranin O staining along with Fast Green and weak hematoxylin counterstaining was performed to stain GAGs orange, non-collagenous proteins green, and cell nuclei deep purple, respectively (Figure 3.13). Similar to H&E staining, nuclei and ECM components were difficult to perceive on hydrogels containing DCC particles. Furthermore, Safranin O dye selectively binds to GAGs such as hyaluronic acid so background staining was predictably evident. However, the 5, 10 and 15% DCC groups in week 4 exhibited regions of high-intensity regions of orange-red, regions, which were not seemingly present in day 1 and week 2 samples. Furthermore, the 15% DCC group seemed to have larger and more intense areas of red, potentially indicating that DCC particles positively influence chondrogenesis and as a result GAG production. Fast Green staining seemed to selectively stain the cartilage-derived particles in the PHA/DCC hydrogel groups, revealing that DCC particles were stably incorporated into the crosslinked HA matrix throughout the culture period.

DAPI and phalloidin fluorescent dyes were employed to better resolve cell morphology and organization on the opaque hydrogels (Figure 3.14). Cells in the 15% DCC + TGF-ß3 group seemed sparser than in the other groups at weeks 2 and 4, though no quantitative methods were performed to determine relative cell numbers during the 4-week study. The cells in all groups adopted a spread, fibroblastic morphology, and with the exception of the positive control group, cells were confluent by week 2 and appeared to increase in number over time.

CONCLUSIONS

The results herein provide preliminary data as to the efficacy of PHA hydrogels enriched with DCC particles for 1) 3D printing with an open-source, syringe-based extrusion tool and 2) stimulating chondrogenesis and cartilage formation *in vitro*. After preliminary printability tests, hydrogel fabricated with high-molecular weight PHA (1 MDa) and a 3 w/v% polymer content was selected as the ideal dispersion medium for DCC microparticles. The incorporation of DCC enhanced the rheological properties of PHA pre-gel for 3D printing, endowing the pre-gel with a yield stress and higher viscosity. The presence of a yield stress strongly correlated to the resolution of the 3D-printed hydrogels, as the interparticle and intermolecular forces provided structure to the fluid at low or negligible shear stresses, which improved the shape fidelity of 3D-printed pre-gel filaments. The mechanical stiffness and strength of PHA hydrogel were also enhanced by the addition of DCC microparticles. Furthermore, there were no statistical differences in mechanical properties between 3D-printed and mold-casted hydrogel groups, indicating that hydrogel printing is a viable fabrication method for creating patient-specific scaffolds. DCC microparticles also mitigated the swelling of PHA hydrogel, which is beneficial for shape preservation in physiological conditions. Lastly, the PHA/DCC hydrogels supported rBMSC survival and proliferation, and have the potential to promote chondrogenesis as evidenced by fold-increases of the chondrogenic gene, SOX9, and increases in GAG production especially at higher concentrations of DCC microparticles.

Chapter 4: Early Prototyping of Patient-Specific Scaffolds for Mandibular Condyle Regeneration

INTRODUCTION

Temporomandibular disorders (TMDs) affect an estimated 30 million individuals nationwide, and are characterized by pain and dysfunction in the temporomandibular joint (TMJ) and surrounding musculature.[86] Many patients with TMDs experience a reduced ability to carry out functions such as talking, chewing and laughing, which greatly diminishes quality of life. Patients with late-stage disorders often require TMJ reconstruction with either costochondral grafts or alloplastic prostheses to alleviate severe pain and improve joint movement. However, TMJ replacements only function to relieve symptoms rather than restore health to the joint. Furthermore, the long-term stability of the replacements is unpredictable, and there is a high incidence of failure necessitating additional surgeries.

To improve clinical outcomes and expand the range of treatment options for late-stage patients, tissue engineering therapies that aim to "restore, maintain and improve tissue function" hold great promise.[87] Of critical importance for tissue engineering is the generation of scaffolds, which serve to support and instruct resident cells to grow and reproduce the envisioned tissue.[88] Scaffold composition and microarchitecture influences cell behavior and differentiation through physical and chemical signaling mechanisms and can be engineered to stimulate different types of tissue growth within discrete regions. In particular, scaffolds that aim to mimic the complexities of native extracellular matrix (ECM) have been shown to elicit enhanced tissue-specific regeneration. In addition, scaffolds must be biodegradable, so that as cells proliferate and secrete ECM, the formation of congruent tissue is not impeded. Scaffolds must also have

interconnected pores to allow for cell infiltration, homogenous cell distribution, and efficient nutrient and waste exchange.[88]

Recently, three-dimensional (3D) printing technologies have been implemented in the field of tissue engineering to enable the digital design and manufacture of more sophisticated scaffold-based therapies.[88, 89] 3D printing uses motorized, multi-axis deposition tools, to extrude material in defined patterns, layer upon layer, to yield specific 3D geometries. This technology allows researchers to not only customize the external macrostructure, but also the internal microstructure of scaffolds, which greatly influences cell differentiation and the mechanical properties. Compared to conventional scaffold fabrication techniques, 3D printing offers significant benefits in that interconnected pore structures can be carefully designed and reproduced to facilitate specific cell-material interactions to more predictably control cell behavior. The internal pore structures of scaffolds fabricated by conventional techniques on the other hand, rely on the randomness of the fabrication process, and are not controllable to a large degree. Furthermore, 3D printing technology in combination with medical imaging enables the creation of scaffolds with patient specificity to restore the anatomic structure of defective tissue as well as the spatial patterning of structural and biological cues to induce site-specific tissue formation.

Computational control over scaffold features, which dictate cell behavior such as cell growth and differentiation, is therefore highly beneficial especially in multi-tissue or interfacial tissue engineering applications. Biological joints are particularly demanding to regenerate since they are composed of bone and cartilage tissues, which differ in cell type, ECM components, ECM organization and mechanical properties. In addition, joints have an interfacial region that exhibits transitional characteristics and serves to stabilize and unite the two disparate tissues. To

produce osteochondral scaffolds for joint regeneration, multiple printing tools can be combined to deposit multiple materials, even within the same layer, to produce both discrete and integrated regions within the scaffold. 3D printing therefore has the potential to integrate materials in multi-tissue scaffolds in a controlled manner to avoid delamination, a recurring problem in osteochondral tissue engineering.[90]

To address the need for further development of tissue engineering therapies for biological joint repair such as the mandibular condyle, extrusion-based 3D printing was used to generate customized scaffolds with cell-instructive biomaterials. A method was devised using readily accessible or open-source software to design anatomically-shaped and porous scaffolds with discrete bone and cartilage regions as well as an interfacial region. Two types of 3D printing tools, fused deposition modeling (FDM) and direct ink writing (DIW), were used to deposit materials in a layer-by-layer fashion to translate the digital model into a scaffold using a customized desktop 3D printer. Monofilament feedstock for FDM was fabricated with polycaprolactone, a biodegradable polymer, and hydroxyapatite nanoparticles, which have been shown to enhance osteogenesis and were used to print the bone region.[91] The chondroinductive region was made with hyaluronic acid-based hydrogel, a constituent of native cartilage, enriched with decellularized cartilage (DCC) microparticles, which have shown great promise in promoting cartilage growth.

PATIENT DATA-DRIVEN SCAFFOLD PRODUCTION

The general method for the computer-aided design and manufacture of patient-specific scaffolds for tissue engineering is depicted in Figure 4.1. First, medical data from computed tomography (CT) or magnetic resonance imaging (MRI) is required in order to acquire

information about the dimensions and shape of the area of interest. The scans are then merged to render a 3D volume so that a surface mesh of the desired subvolume can be created. Once generated, the mesh is repaired to remove non-manifold elements to ensure that it is watertight. Next, the mesh is converted into a solid base feature so that it can be modified with CAD modeling software to introduce an interconnected pore structure and design additional scaffold features. Once finalized, the model is exported as an STL file and translated into G-code, through the use of 'slicing' software, which slices the model into layers and defines the printer movements and tool path within each layer. To generate G-code that yields high-quality printed objects, printing parameters within the slicing software such as extrusion temperature and printing speed among others must be sufficiently defined for each material. After the G-code script is generated, the script is sent to the printer and the line-by-line commands are executed until the 3D scaffold is fully realized. In addition to selecting adequate printing parameters, the printing process is also highly dependent on the mechanical printer calibrations as well as the physical properties of the material feedstock. Once printed, the 3D-printed scaffold and the CAD model are compared, and if discrepancies are observed, printing parameter adjustments, biomaterial development, hardware modifications, printer calibrations, or model redesigns are performed. This process is highly iterative and the quality and resolution of the scaffold rely on the interdependency of technical, structural and material factors. Additionally, the software toolchain, which is the list and order of software programs used to translate 2D medical scans into 3D-printed scaffolds, is summarized in Figure 4.2. All of the software employed in this investigation was either free or open-source, and is listed beneath the software toolchain flow chart.

MATERIALS AND METHODS

Scaffold Design

CT Data Processing/Mesh Creation

CT imaging was performed on a porcine head to acquire DICOM files, which capture and store the 2D scans (Figure 4.3A). 3D Slicer, an open-source medical image processing software, was used to convert the 2D medical scans into a 3D surface model of the mandibular condyle, which is a format suitable for import into CAD modeling software (Figure 4.3B). After the DICOM data were loaded, bone regions were isolated and rendered to visualize the 3D volume by defining the intensity threshold. The 3D rendering was then cropped to encompass the left mandibular condyle, and a label map based on intensity and location was created to differentiate the temporal region from the mandibular region of the TMJ in order to trim away superfluous tissue.[92] Once each region was labeled and segmented, the mandibular region was selected and a surface model or mesh of that segment was generated and exported in an STL file format.

Mesh Repair

Once an STL file of the mandibular condyle was obtained from the CT data, the surface mesh was processed and fixed to repair surface holes, make the mesh manifold, remove floating surfaces, and reduce the number of faces to below 10,000 for successful upload into Autodesk Inventor, a CAD modeling software. A series of open-source software programs were used in combination to re-mesh the surface model to a satisfactory level. MeshLab was used to re-orient the mandibular condyle and remove holes and nonmanifold elements. Netfabb Basic was used to crop the mandibular condyle to produce cleaner geometries, and remove extraneous surfaces and

other noise. Lastly, Autodesk Meshmixer was used to reduce the number of faces and smooth the surface of the condyle to remove topographical errors (Figure 4.3C).

CAD Modeling

The fixed STL file was imported into Autodesk Inventor and the mesh data was converted to a solid base feature with the Mesh Enabler plugin (free for students). Pore channels were introduced to create struts 0.5 mm in width, which is the minimum allowable width for the 0.5 mm extrusion nozzle, and 0.9 mm in height corresponding to three printed layers with heights of 0.3 mm. Since layer height must be less than 80 percent of the nozzle size (according to a heuristic), a layer height of 0.3 mm is considered acceptable. The pore channels were 600 μm in width and 900 μm high, which lies within the ideal pore size range for osteoinductive scaffolds (greater than 300 μm for bone growth and vascularization and between 500-1000 μm to stimulate proliferation).[93, 94] The pores were interconnected and placed in 0-90 degree orientations to increase cell seeding, enable homogenous cell distributions, and facilitate efficient nutrient transport.[59, 88]

Since the CT scan data does not resolve condylar cartilage, a cartilage region was designed through direct graphical manipulation of the mesh using Autodesk Meshmixer. The surface of the condyle was offset by 2 mm to mimic the height of native condylar cartilage, and the soft transition function was applied to establish continuity between the offset surface and underlying condylar body. To further enhance the design, the sculpt function was used to perform manual reshaping, and the smooth function was used to simplify the mesh representing the condylar surface. After edits were made, the model was exported as an STL file, imported into Autodesk Inventor, and converted to a solid base.

To create the cartilage region, an independent bone region was created that, when subtracted from the sculpted model through Boolean operations, produced a cartilage region that was solid above the interface and that enmeshed with the bone region below the interface. The cartilage region was designed to extend into the top three strut layers of the bone region to anchor the hydrogel into the thermoplastic-based region and prevent delamination. In this region, the spacing between the struts of the bone region was enlarged to 0.9 mm to accommodate insertion of the dispensing tip for hydrogel deposition within the confines of the thermoplastic-based struts. Once both regions were created they were exported as individual STL files for upload into Slic3r, a slicing software, for G-code generation. The finalized scaffold design is displayed in Figure 4.3D.

Hardware Development

An extrusion tool was built and attached to an existing RepRapPro Mendel Tricolor 3D Printer to enable the co-deposition of fluids and thermoplastic-based filaments for the creation of complex, multi-material structures. The open-source extrusion tool was constructed from 3D-printed parts to enable motor-controlled linear actuation of 10-mL syringes. Through the displacement of the syringe plunger, fluidic materials were driven through tubing and an 18-gauge dispensing tip, which was secured to the motorized print head to allow for the deposition of fluids in programmed patterns. The syringe-based extrusion tool in combination with a UV lamp attachment provided the means to print photocurable hydrogels in the present study. For further details on the syringe-based extrusion tool and 3D printer setup see Chapter 3. In addition, the 3D printer was equipped with two Bowden-style extruders, which were mounted to the frame of the 3D printer and drive filament through stiff tubing and into heated nozzles

located on the motorized print head. The customized 3D printer therefore has the capacity to print with two filaments and one fluidic material to construct multi-material 3D objects. Lastly, Kapton tape was applied to the surface of the print bed to facilitate first-layer adhesion, and is a common practice in FDM.

Biomaterial Development

Osteoinductive 'Ink' Development

Monofilament Production

Various thermoplastic-based monofilaments were produced for 3D printing with the FDM extrusion tool. The following thermoplastic monofilaments were attempted with a single-screw extruder: 14 kDa-PCL, 80 kDa-PCL and PLA, 14 kDa-PCL + 5 wt% HAnp, 80 kDa-PCL + 5 wt% HAnp, PLA + 5 wt% HAnp. Unless otherwise stated, all materials were purchased from Sigma-Aldrich. To make PCL + 5 wt% HAnp monofilaments, PCL pellets and 5 wt% hydroxyapatite nanopowder were combined and melted in an oven at 75°C with occasional stirring to achieve a consistent mixture. Once cooled, the composite materials were manually granulated into pellets with approximate sizes of 3-5 mm. The pellets were then extruded through an annular die with a diameter of 1.65 mm using a single-screw extruder (Filabot Original Filament Extruder, Barre, VT) at a temperature of 95°C. Once extruded, a cooling fan was used to facilitate rapid solidification to ensure that the cross-section remained circular with a consistent diameter of 1.75 mm for input into the Bowden extrusion tool. For PLA + 5 wt% HAnp monofilament production, compounding was carried out at 220°C, and PLA-based pellets were extruded at 235°C through a 1.95 mm annular die to produce monofilaments roughly 1.75 mm in diameter.

Monofilament Printing

Once pure polymeric and composite monofilaments were prepared, they were threaded into the Bowden extrusion tool and extruded at 100 mm/min. The nozzle temperature was set to 220°C for PLA-based filaments and 110°C for PCL-based filaments. However, none of the filaments produced with the single-screw extruder were tolerated by the 3D printer. Every filament caused the extrusion tool to jam, and the tool had to be dismantled and rebuilt after each blockage. To address this limitation, alternative 3D printing methods for patient-specific scaffold production with thermoplastic/HAnp composites, such as indirect 3D printing and solvent printing, were investigated.

Indirect 3D Printing

Indirect 3D printing methods were employed to construct a shape-specific bone region with CAD-generated pore architecture using PCL and 5 wt% HAnp. First, a negative or inverse 3D model of a cylinder with interconnected microchannels was designed where the voids in the sketch corresponded to the overall structure of the scaffold. Next, the negative mold was printed at 228°C with a printing speed of 15 mm/s using polystyrene filament (MatterHackers, Orange County, CA). PCL powder with 5 wt% HAnp was loaded into the mold and raised to 80°C to melt the PCL. Once melted, more material was packed and tamped down into the mold to ensure uniform loading and an even distribution of material throughout. The sacrificial mold containing the hardened PCL and HAnp cast was selectively removed through dissolution in Citra Solv, leaving the insoluble PCL/HAnp structure.

Solvent Printing

To test the feasibility of printing PCL/HAnp structures with the syringe-based extrusion tool, PCL dissolved in dichloromethane (DCM) containing HAnp suspensions was loaded into a syringe and extruded. First, 0.33 g of HAnp were added to 8.25 mL of dichloromethane (DCM) and sonicated until a stable suspension was achieved. In parallel, 3 g of PCL was dissolved in 100 mL of DCM, and then mixed with the HAnp suspension. The mixture was then loaded into Luer-Lok syringes to test syringe-based extrusion through 20- and 18-gauge dispensing tips. After extrusion onto a surface, the solvent was allowed to evaporate to yield a stable PCL/HAnp deposit, and the remaining extrudate was qualitatively assessed.

Chondroinductive 'Ink' Preparation

In Chapter 3, hydrogels comprised of PHA and DCC microparticles were optimized to construct multilayered 3D hydrogels with the current 3D printer system. Based on findings, 3 w/v% 1 MDa-PHA hydrogel precursor solution with suspensions of 15 w/v% DCC microparticles was arguably superior to other tested chondroinductive 'ink' formulations as it yielded the highest-resolution 3D hydrogel structures. Moreover, the crosslinked hydrogels were shown to support cell growth, and possessed chondroinductive potential. Previously described protocols were used to synthesize PHA and DCC microparticles. In brief, PHA was synthesized by reacting hyaluronic acid with a 5-fold molar excess of pentenoic anhydride in a 3:2 v/v ratio of water to DMF maintained at a pH of 8 to 9 under continuous stirring to yield degrees of functionalization ranging from 22-28% as verified through ^{H}NMR spectroscopy. DCC microparticles were prepared by first harvesting articular cartilage from porcine knees. Once harvested, cells and immunogenic epitopes were removed through a multistep process involving

tissue fragmentation, enzymatic breakdown, osmotic shock, and detergent and solvent washes. Through double-stranded DNA quantification, 76% of the cells were removed. The resulting decellularized matrix was further processed with a cryogenic mill to pulverize the DCC to micron-sized particles. To prepare the chondroinductive ink, 150 mg of PHA, 58.44 mg of dithiothreitol (DTT), and 750 mg of DCC were mixed with 5 mL of PBS containing 2.5 mg of dissolved Irgacure 2959. The mixture was then centrifuged to remove air bubbles and was loaded into a 10 mL Luer-Lok syringe for printing with the syringe-based extrusion tool.

Scaffold Manufacture

The individual mesh designs of the respective bone and cartilage regions were uploaded in STL file formats into Slic3r, an open-source slicing software, where the meshes were converted into line-by-line printer instructions in the form of G-code based on complex algorithms and user-defined print settings. Subsequently, the G-code script was modified to achieve acceptable 3D-printed objects with the syringe-based extrusion tool as described in Chapter 3. The G-code was then forwarded to the Marlin firmware, which is located on the printer controller board, through the host interface software, Pronterface. All software programs used in scaffold prototyping were either free to students or open-source downloads from the Internet. Once the print job was initiated and the G-code commands were executed to produce a 3D-printed object, the overall build quality and dimensional accuracy of the object was evaluated. Based on these output evaluations, parameters were adjusted in Slic3r to enhance the overall quality of the product. Printing parameters are dependent on the hardware, software and printing material, and substantial deviations in printing parameters are expected when the 3D

printing technique, print design or feedstock material is changed. Therefore, care must be taken to select suitable parameters through iteration for the construction of novel 3D designs.

To produce the bone region of the scaffold, FDM was used to print commercial monofilament (PCL or PLA) to validate model production by 3D printing. Each thermoplastic filament was loaded into the Bowden extrusion tool and printed at various temperatures and defined printing parameters to achieve suitable build dimensions and features. PCL and PLA from MakerBot were used to print the bone region of the scaffold to validate the model. Composite and commercial PCL filaments were not suitable for printing, and will be discussed in further detail in subsequent sections. PLA was therefore used to print the bone region during biphasic scaffold production to demonstrate proof-of-concept. The cartilage compartment was printed with 3 w/v% PHA and 15 w/v% DCC hydrogel ink with the syringe-based extrusion tool and the bone compartment was printed with the Bowden-style extruder. The model design was cropped to contain only the top three strut layers of the bone region and the cartilage overlay to evaluate the co-deposition of materials with the 3D printing system and to qualitatively assess the integration of the two dissimilar materials in the interfacial region of the scaffold.

RESULTS

Custom-Made Filament Evaluation

Filaments were produced with a Filabot Original Filament Extruder by adjusting the extrusion temperature and annular die diameter to yield an approximate filament diameter of 1.75 mm. In addition, a cooling fan was aimed at the outlet nozzle to accelerate material solidification once extruded to improve shape fidelity and dimensional accuracy. Once steady-state extrusion was attained, the filament was collected in coils at ground level and the width was

measured at different locations along the length of the filament to evaluate cross-sectional uniformity. Visual or qualitative assessments were also performed to inspect for inconsistencies in appearance.

Filament production using 15 kDa-PCL flakes and 15 kDa-PCL + 5% HAnp pellets was attempted, but the materials did not extrude as continuous filaments. Rather, the material was extruded out in small grainy masses. 80 kDa-PCL filaments when extruded tended to puff out at the outlet of the die, but dramatically thinned to the point of breakage as the filament was driven outward since rapid hardening did not occur despite the presence of a cooling fan. Even at the lowest extrudable temperature of 65°C, the extrudate had a melted appearance and poor shape retention. Extrusion was even carried out in refrigerated conditions to help secure the shape of the filament once extruded, but the cooling fan alone proved to be equally as effective. To diminish filament thinning and subsequent breakage, a basin of deionized water was placed just under the extruder outlet to facilitate rapid cooling and solidification of the filament. This method was effective at stabilizing the extruded filament, but with this setup the filament had to be manually collected, which introduced slight defects in the filament upstream of the perturbations, and steady state conditions were unattainable. With this method, a die size of 1.65 mm was selected to produce PCL-based filaments with widths of ~1.75 mm. In contrast, PLA-based filaments cooled rapidly once extruded, which obviated the need for immediate entry into a cooling bath. The cooling fan alone was enough to stabilize the extruded PLA-based filament. The extrusion temperatures for PLA and PLA + 5% HAnp were 205 and 215°C, respectively; however, the material once extruded took on a discolored or burned appearance.

Extrudability tests with filament removed from the region of steady state production was loaded into the Bowden extrusion tool and was extruded at 100 mm/min to determine whether

filaments made in-house could be tolerated by the 3D printing system. However, none of the filaments were able to achieve consistent extrusion. Where the filament was too thin, the idler and toothed gear did not provide enough tension to drive the filament through the Bowden tubing and heated extrusion nozzle. Where the filament was too thick, it either jammed the idler, causing the stepper motor to jam, or blocked the tubing or extrusion nozzle. With filament jams and blockages, the extrusion tool had to be dismantled and rebuilt. Also, the tool could not handle bends in the filament or any inconsistencies that deviated from 1.75 mm within a slim margin as they would also jam the tool. The allowed variation for many FDM filaments is 1.75 ± 0.05 mm, though no number could be verified for the current 3D printer. Variations in filament diameter not only limit extrusion, but also if printable, introduce variation into the printed part in terms of size and strength.[95] To improve the filament making process, speed control, real-time measurements of the filament diameter with a laser micrometer, and a steady state filament collection or coiling method would go a long way in minimizing the variation to within the acceptable tolerance.

For composite filaments, the added complication of manual compounding and granulating was undesirable, as it was difficult to manually incorporate HAnp into the melted thermoplastics. PCL with 10% HAnp was attempted, but the powder could not be pounded into the material at that concentration by hand as the molten thermoplastic was too viscous. Therefore, 5% HAnp was used for proof-of-concept.

Bone Region Construction

Direct 3D Printing

The bone region of the scaffold was printed with thermoplastic-based filaments to confirm that the model could be translated into an equivalent 3D structure with an FDM extrusion tool and to determine valid print and material settings for biphasic scaffold production. 38 layers were printed in total with heights of 0.3 mm and alternating 0-90° rectilinear infill patterns that together formed a crosshatched internal architecture with an external shape of the porcine mandibular condyle head and neck. Since the 3D printing system could not tolerate the dimensional inconsistencies of filaments made in-house, commercial PCL and PLA filaments were used to prove feasibility. Printing parameters were adjusted in the slicing software to achieve accurate, high-quality scaffold features. For PCL filament, considerable parametric optimization was performed changing critical parameters such as printing speed, extrusion volume, extruder temperature, build plate temperature, interlayer cooling times, infill pattern, infill density and various retraction factors, but scaffolds could not be produced. Print tests with dissolvable support structures were also attempted to improve the deposition of PCL in crosshatched layers, but porous structures could not be manufactured. The eventual failure of all test prints was due to ghosting, where extruded material was not deposited onto the previous layer. This ghosting phenomenon was thought to be due to inconsistent extrusion with the FDM extrusion tool. Though PCL exhibited good layer adherence when deposited on solid surfaces, PCL was not able to form crosshatched or porous structures. The material would not form bridges over void spaces, but rather the material preferentially adhered to the nozzle head forming misshapen globules that were irregularly deposited onto the printed object. Since other groups have successfully manufactured porous PCL scaffolds with void spaces and even more

intricate porous designs using 3D printing technologies, these production challenges were thought to be due to the method of printing itself.[70, 96] Since PCL is flexible, there are significant difficulties in printing intricate structures with a Bowden-style extruder, which does not have sufficient pressure to push flexible filament through the hot end. When driven through the tubing, the filament flexes rather than forces itself through the hot end, thereby causing deviations in extrusion volume, which introduces errors into the 3D-printed structure. 3D printing forums have corroborated this phenomenon, and Bowden-style extrusion is therefore not recommended for use with flexible filaments. Other extrusion techniques such as direct or pneumatic extrusion as well as other 3D printing techniques such as selective laser sintering have been used to successfully manufacture PCL scaffolds with porous internal architectures, and could instead be employed.

In addition to ghosting, substantial stringiness and areas of warping were observed in PCL prints. Since the melting temperature of PCL is low (~65°C), PCL does not immediately harden upon extrusion like PLA or ABS thermoplastics, which have high melting temperatures (~200 and 230°C, respectively). PCL is instead viscous after deposition and the structural instability of melted PCL leads to flattening, thereby distorting the overall print. Therefore, it was determined that a cool down time of at least 90 seconds should be implemented in between layers to enable solidification to prevent warping and to support the next print layer.

PLA, a widely available and commonly used thermoplastic for conventional FDM techniques, was used to print the bone region design.[97] The scaffold was printed at an extrusion temperature of 215°C, and a print speed of 15 mm/s. The resulting 3D-printed structure closely matched the model and programmed deposition path and was nearly identical to the model in shape, dimension and pore size (Figure 4.4).

Even though HAnp was not incorporated in the prototype, there is evidence to suggest that 3D-printed scaffolds constructed of pure commercial PLA filament alone can promote osteogenesis through the incorporation of biomimetic microstructures.[90] Preliminary data suggest that PLA microstructures that mimic the architectural properties of bone, such as concentric circles, in the absence of other bioactive factors can support cellular adhesion and promote osteogenesis through purely structural cues.[90] Employing biomimetic structural features may therefore be one approach in overcoming the need for composite filament. However, two other methods were investigated as workarounds to construct well-defined PCL/HAnp scaffolds while avoiding the need for composite monofilaments.

Indirect 3D Printing

To overcome technical and material constraints of patient-specific scaffold production with PCL and hydroxyapatite additives using FDM, indirect rapid prototyping was investigated. Sacrificial molds were designed with CAD software and printed with polystyrene filament followed by traditional melt casting of osteoinductive composite material to establish a shape-specific external structure and user-designed interconnected pore channels. The indirect 3D printing process is shown in Figure 4.5, in which an inverse model was designed, printed and dissolved to yield a cylindrical scaffold with interconnected pores comprised of PCL and HAnp. The scaffold was successfully created to exact specifications and is a promising approach for single tissue engineering since well-defined scaffolds can be fabricated using materials that are otherwise unacceptable for direct 3D printing. This approach employs 3D printing to create molds with highly printable, commercially available filament that yield high-resolution casts of novel biomaterials, which may be otherwise difficult to attain through direct 3D printing. Since

indirect 3D printing enables the production of scaffolds with composite biomaterials to precise specifications, the need for novel filament fabrication is obviated. This approach is promising and several researchers have employed indirect 3D printing for osteochondral tissue engineering.[98] However, these studies typically manufacture the bone and cartilage regions separately and use fibrin glue or sutures to adhere the two regions, which oftentimes leads to a structurally weakened interface and subsequent delamination.[90] Direct 3D printing in contrast enables the sequential deposition of materials so that two materials can be deposited in customized patterns within the same layer to better integrate the materials and reinforce the interface to ensure long-term success and resistance against deformation. Although a viable option, direct 3D printing has apparent advantages over an indirect approach in generating well-integrated osteochondral scaffolds for biological joint regeneration.

Solvent Printing

The feasibility of direct 3D printing with stable HAnp suspensions in PCL solution was examined by extruding PCL/HAnp in DCM through a 10-mL Luer lock syringe equipped with an 18-gauge dispensing tip onto paper. The solution deposited smoothly onto the paper and the solvent appeared to evaporate within 5 minutes leaving patterned residues of PCL and HAnp. Manual syringe extrusion before and after solvent evaporation is shown in Figure 4.6. From macroscopic observation, the extrudates shrunk along all axes after solvent evaporation and exhibited moderate changes in shape and dimension. While PCL and HAnp in solvent can be extruded as continuous filaments by a syringe, devising a process to produce scaffolds with this mixture using the syringe-based extrusion tool may be challenging. Advanced design strategies and customized G-code would be required to account for evaporation and the accompanied

changes in shape and dimension of the deposited material. While solvent printing offers flexibility and versatility by allowing for direct 3D printing of novel composite materials, methodologies would have to be extensively developed in order to create reproducible prints.

Biphasic Scaffold Design and Manufacture

The biphasic scaffold design was cropped to evaluate the feasibility of constructing a multilayered scaffold in the anatomical shape of a porcine condylar head with well-integrated bone and cartilage regions by co-depositing PLA filament and 3% PHA + 15% DCC hydrogel ink with the customized 3D printer. The complex scaffold consisted of a bone region with 600 – 900 μm pore channels to facilitate transport of nutrients and waste and a cartilage region, which resided on the superior surface of the condylar head and was designed to match dimensions found in literature. To integrate the two regions, chondroinductive ink was deposited in between the PLA struts for 3 strut layers to anchor the hydrogel into the thermoplastic lattice to prevent delamination. Before printing the model, the two extrusion tools employed in the printing job (syringe-based and FDM extruders) were carefully offset and defined in Slic3r to enable dual-printing and to equilibrate the coordinates. Printing this scaffold however proved challenging. The hydrogel did not deposit smoothly in between the struts of the bone region, causing broad dispersal of hydrogel across the surface. In addition, the hydrogel was destroyed during printing due to the high processing temperatures of PLA. When printing upon layers containing hydrogel, the hot end extruder nozzle caused the hydrogel in close proximity to singe and brown. Due to these occurrences, the prints were messy and were not successfully executed. Furthermore, tool switching caused a lot of odd behaviors that were not implicit in the G-code script. Most notably, communication between the host interface software and the controller board was often lost when

tool changes were made. Consequently, printer movements would stop indefinitely and the print could not be salvaged or reset. As a result, a low percentage of prints actually made it to completion.

DISCUSSION

The production of patient data-driven scaffolds with osteo- and chondroinductive biomaterials with CAD/CAM technologies relies on the interdependence of hardware and software capabilities, the complexity and translatability of the scaffold design, and the ease in which the biomaterials can be processed. Therefore, hurdles in any one of these areas can negatively affect or compromise the feasibility of scaffold production entirely. This work marks the beginning of developing an approach to print with both thermoplastic-based filament and hydrogel to construct a multilayered scaffold with separate bone and cartilage compartments and an integrated interface to promote mandibular condyle regeneration. However, many limitations need to be overcome to further advance this therapy.

First, since the implementation of 3D printing for tissue engineering applications is still emerging, there is a shortage of biomaterials available for 3D printing. Therefore, printable biomaterials must be newly engineered or established biomaterials must be adapted for 3D printing, specific to the printing technique employed. The current study aimed to adapt an established osteoinductive biomaterial, PCL with apatite additives, for printing with an open-source desktop 3D printer using a Bowden extrusion tool. This was accomplished by the fabrication of composite filament. However, the 3D printer could not tolerate the slight cross-sectional inconsistencies of composite filaments produced in-house. Aside from attempting to improve the diametric consistency by altering the extrusion temperature, molecular weight of the

polymer, method of collection, and cooling arrangement, indirect 3D printing and direct 3D printing of PCL and HAnp in solution were considered in order to bypass filament production altogether. While both approaches seemed to enable scaffold production with PCL and HAnp, both methods have their individual advantages and disadvantages. Indirect 3D printing is highly advantageous in that it can facilitate the production of CAD-designed scaffolds with biomaterials that are otherwise unprintable. In this process, melted biomaterial is cast into a 3D-printed sacrificial mold and the final scaffold is retrieved by selective dissolution of the mold. While this method provides a certain level of control over the external geometry and internal pore structure of the scaffold, it prevents the patterning of multiple materials within the same plane of the scaffold, which is not ideal for multi-tissue or interfacial tissue engineering applications. In contrast, solvent printing enables multiple materials to be deposited within single layers of the scaffold in a controlled manner. However, solvent evaporation changes the structure and dimensions of the depositions. While this method also circumvents the need for novel, composite filaments, advanced methodologies would need to be developed to account for solvent evaporation and associated shrinkages of the print in order to produce a scaffold that correlates to the CAD model.

Another limitation that impeded scaffold production lied in the mechanics of the filament extrusion tool. The Bowden-style extrusion tool was unable to drive consistent volumes of PCL through the heated nozzle, which translated into large discrepancies in the printed structure, leading to either immediate or eventual print failure. For Bowden-style extrusion, filament must be pushed through both tubing and a heated nozzle by a remote stepper motor. However, due to the innate flexibility of PCL, the filament tended to buckle within the tubing rather than progress through the nozzle, causing inconsistent extrusion. To overcome this hurdle, a 3D-printer

equipped with a direct extruder or a temperature-controlled pneumatic or syringe-based extruder could be used. Theoretically, the Bowden set-up could also be rebuilt with highly restrictive parts to prevent the PCL filament from flexing.

Furthermore, extensive optimization needs to be performed to construct regions containing both hydrogel and thermoplastic-based materials within the same layer. During multi-material prints, deposited hydrogels were scorched beyond repair due to run-ins with the heated nozzle of the filament extruder. One way to avoid hydrogel scorching would be to improve the positioning accuracy of the print head to achieve more precise movements and prevent contact between the heated nozzle and printed hydrogel. Moreover, the resolution and overall extrusion quality of the hydrogel ink was unacceptable. When the hydrogel ink was dispensed in between the thermoplastic struts of the bone region, the hydrogel neither formed continuous strands nor remained within the struts. The messiness of the hydrogel depositions in large part is thought to be due to the rudimentary nature of the custom-built syringe-based extruder. The extruder can not produce high-resolution filament strands and also experiences significant material leakage out of the dispensing tip during prints. This leakage not only causes issues in maintaining consistent extrusion volumes, but also leads to random droplets of material falling onto the printed object. An extrusion tool, either pneumatically or piston-driven, with a valve to prevent unwanted flow of material would therefore be highly desirable.

Lastly, due to the open-source nature of these 3D printing technologies, consistent technical glitches and reliability issues were encountered.

CONCLUSIONS

Scaffold prototyping is a highly iterative process that relies on the interdependency of its four main stages: design, manufacture, biomaterial development and hardware development. The above study endeavored to design porous, osteochondral scaffolds based on patient data with cartilage and bone regions and an integrated interfacial region for manufacture with DIW and FDM techniques. Osteoinductive feedstock development for FDM was also explored; though composite filaments were unusable as they contained cross-sectional inconsistencies that were not tolerated by the extrusion tool. For proof-of-concept, the osteochondral scaffold design was printed with 3% PHA + 15% DCC hydrogel ink for the cartilage region and PLA thermoplastic for the bone region. However, due to intrinsic limitations in material processing and the mechanics of the extrusion tool, further advancements are required to feasibly produce the patient-specific osteochondral scaffolds.

Chapter 5: Conclusions and Future Directions

This thesis marks the early development of patient-specific osteochondral scaffolds composed of hydrogel and thermoplastic-based materials using combined 3D printing techniques. First, chondroinductive hydrogel 'ink' was developed as the material feedstock for syringe-based extrusion. Pentenoate-modified hyaluronic acid (PHA) pre-gel enhanced with decellularized cartilage (DCC) microparticles, showed favorable rheological properties for 3D printing, having observable yield stresses, shear-thinning behavior and high yet tolerable viscosities. In a concentration-dependent manner, DCC microparticles enhanced the structure of PHA pre-gel and crosslinked PHA hydrogel networks due to increased interparticle forces, which improved both the resolution, and mechanical stiffness and strength of the 3D-printed structures. Furthermore, the compressive mechanical properties of 3D-printed and mold-casted hydrogels were not statistically different, revealing that the layer-by-layer patterning of hydrogels does not reduce the mechanical integrity of the overall structure. Lastly, hydrogels with higher concentrations of DCC were shown to stimulate larger fold-increases of certain chondrogenic gene markers *in vitro*, signifying chondroinductive potential.

To further characterize PHA/DCC hydrogel for potential use in acellular joint regeneration therapies, cell infiltration should be studied in 3D-printed gels to investigate whether endogenous progenitor cells from the bone marrow can penetrate and remodel the hydrogel network. In addition, implantation into an animal model would be useful to evaluate the efficacy of 3D-printed PHA/DCC hydrogels to regenerate cartilage *in vivo*. To further enhance the hydrogel to function as a cartilage substitute prior to tissue ingrowth, the mechanical properties must be increased to have similar magnitudes to those of native cartilage so that the hydrogel can withstand physiologically relevant loads. To improve the mechanical properties,

the crosslinking density can be increased or structural thermoplastic lattice structures could be co-deposited within the hydrogel scaffold to improve mechanical robustness.

The discrete bone region of the scaffold should also be optimized and characterized. First, a method must be to devised to produce consistent filaments with inherent osteoinductive potential for FDM. Additionally, pore shape, size and organization should be investigated to produce scaffolds that through mechanotransduction elicit osteogenesis and bony ingrowth. More complex microarchitectures, which mimic the structural features of bone, should also be considered.

Lastly, open-source software platforms were used to convert medical informatics into digital models representing the anatomical shape of the mandibular condyle, which were successfully modified with CAD techniques to yield patient-specific scaffolds. However, significant constraints were imposed in the manufacture of this design. The following improvements must therefore be employed in order to further advance this technology:

- Higher resolution hydrogel printing tool with valve to prevent drips
- Method to produce consistent 1.75 mm composite filament to enable PCL/HAnp printing
- 3D printer that can support direct rather than Bowden-style filament extrusion for flexible filament printing
- Commercially developed software and hardware tooling to bypass technical glitches and reliability issues
- Advanced G-code algorithms or development of extensive manual scripts to optimize printer instructions and tool paths for scaffold production with novel biomaterials

References

1. Jakus, A.E., Rutz, A.L. & Shah, R.N. Advancing the field of 3D biomaterial printing. *Biomedical Materials* **11**, 014102 (2016).

2. Athanasiou, K.A., Almarza, A.J., Detamore, M.S. & Kalpacki, K.N. Tissue Engineering of Temporomandibular Joint Cartilage. (Morgan and Claypool Publishers, 2009).

3. Allen, K.D., Detamore, M.S., Almarza, A.J. & Athanasiou, K.A. in Wiley Encyclopedia of Biomedical Engineering. (ed. M. Akay) (Wiley Publishing, Hoboken, NJ; 2006).

4. Detamore, M.S., Athanasiou, K.A. & Mao, J. A call to action for bioengineers and dental professionals: directives for the future of TMJ bioengineering. *Ann Biomed Eng* **35**, 1301-1311 (2007).

5. Tanaka, E., Detamore, M.S. & Mercuri, L.G. Degenerative disorders of the temporomandibular joint: etiology, diagnosis, and treatment. *J Dent Res* **87**, 296-307 (2008).

6. Mercuri, L.G. Alloplastic temporomandibular joint reconstruction. *Oral Surg Oral Med Oral Pathol Oral Radiol Endod* **85**, 631-637 (1998).

7. Wang, L. & Detamore, M.S. Tissue engineering the mandibular condyle. *Tissue Eng* **13**, 1955-1971 (2007).

8. Wolford, L.M., Mercuri, L.G., Schneiderman, E.D., Movahed, R. & Allen, W. Twenty-year follow-up study on a patient-fitted temporomandibular joint prosthesis: the Techmedica/TMJ Concepts device. *J Oral Maxillofac Surg* **73**, 952-960 (2015).

9. Ware, W.H. & Taylor, R.C. Cartilaginous growth centers transplanted to replace mandibular condyles in monkeys. *J Oral Surg* **24**, 33-43 (1966).

10. Ware, W.H. & Taylor, R.C. Growth center transplantation to replace damaged mandibular condyles. *J Am Dent Assoc* **73**, 128-137 (1966).

11. Poswillo, D.E. Biological reconstruction of the mandibular condyle. *Br J Oral Maxillofac Surg* **25**, 100-104 (1987).

12. MacIntosh, R.B. in Surgical Correction of Dentofacial Deformities: New Concepts., Vol. III. (ed. B. W.H.) 355-410 (Saunders, Philadelphia; 1985).

13. MacIntosh, R.B. The use of autogenous tissues for temporomandibular joint reconstruction. *J Oral Maxillofac Surg* **58**, 63-69 (2000).

14. MacIntosh, R.B. & Henny, F.A. A spectrum of application of autogenous costochondral grafts. *J Maxillofac Surg* **5**, 257-267 (1977).

15. Obeid, G., Guttenberg, S.A. & Connole, P.W. Costochondral grafting in condylar replacement and mandibular reconstruction. *J Oral Maxillofac Surg* **46**, 177-182 (1988).

16. Samman, N., Cheung, L.K. & Tideman, H. Overgrowth of a costochondral graft in an adult male. *Int J Oral Maxillofac Surg* **24**, 333-335 (1995).

17. Ellis, E., 3rd, Schneiderman, E.D. & Carlson, D.S. Growth of the mandible after replacement of the mandibular condyle: an experimental investigation in Macaca mulatta. *J Oral Maxillofac Surg* **60**, 1461-1470; discussion 1470-1461 (2002).

18. Guyot, L. et al. Long-term radiological findings following reconstruction of the condyle with fibular free flaps. *J Craniomaxillofac Surg* **32**, 98-102 (2004).

19. Guyuron, B. & Lasa, C.I., Jr. Unpredictable growth pattern of costochondral graft. *Plast Reconstr Surg* **90**, 880-886; discussion 887-889 (1992).

20. Marx, R.E. in Modern Practice in Orthognathic and Reconstructive Surgery, Vol. II. (ed. W.H. Bell) 1448 (Saunders, Philadelphia, PA; 1992).

21. Perrott, D.H., Umeda, H. & Kaban, L.B. Costochondral graft construction/reconstruction of the ramus/condyle unit: long-term follow-up. *Int J Oral Maxillofac Surg* **23**, 321-328 (1994).

22. Svensson, B. & Adell, R. Costochondral grafts to replace mandibular condyles in juvenile chronic arthritis patients: long-term effects on facial growth. *J Craniomaxillofac Surg* **26**, 275-285 (1998).

23. Ross, R.B. Costochondral grafts replacing the mandibular condyle. *Cleft Palate Craniofac J* **36**, 334-339 (1999).

24. Ko, E.W., Huang, C.S. & Chen, Y.R. Temporomandibular joint reconstruction in children using costochondral grafts. *J Oral Maxillofac Surg* **57**, 789-798; discussion 799-800 (1999).

25. Peltomäki, T., Vähätalo, K. & Rönning, O. The effect of a unilateral costochondral graft on the growth of the marmoset mandible. *J Oral Maxillofac Surg* **60**, 1307-1314; discussion 1314-1305 (2002).

26. Peltomäki, T. & Rönning, O. Interrelationship between size and tissue-separating potential of costochondral transplants. *Eur J Orthod* **13**, 459-465 (1991).

27. Peltomäki, T. Growth of a costochondral graft in the rat temporomandibular joint. *J Oral Maxillofac Surg* **50**, 851-857; discussion 857-858 (1992).

28. Pinson, M.L., Coop, C.A. & Webb, C.N. Metal hypersensitivity in total joint arthroplasty. *Ann Allergy Asthma Immunol* **113**, 131-136 (2014).

29. Hallab, N. in Temporomandibular Joint Total Joint Replacement – TMJ TJR – A Comprehensive Reference for Researchers, Material Scientists and Surgeons. (ed. L.G. Mercuri) (Springer, New York, NY; 2016).

30. Granchi, D., Cenni, E., Giunti, A. & Baldini, N. Metal hypersensitivity testing in patients undergoing joint replacement: a systematic review. *J Bone Joint Surg Br* **94**, 1126-1134 (2012).

31. Dormer, N.H., Busaidy, K., Berkland, C.J. & Detamore, M.S. Osteochondral interface regeneration of rabbit mandibular condyle with bioactive signal gradients. *Journal of Oral and Maxillofacial Surgery* **69**, e50-e57 (2011).

32. Talaat, W., Al Bayatti, S. & Al Kawas, S. CBCT analysis of bony changes associated with temporomandibular disorders. *Cranio*, 2151090315Y0000000002 (2015).

33. Di Luca, A., van Blitterswijk, C. & Moroni, L. The Osteochondral Interface as a Gradient Tissue: From Development to the Fabrication of Gradient Scaffolds for Regenerative Medicine. *Birth Defects Research Part C-Embryo Today-Reviews* **105**, 34-52 (2015).

34. Wilkes, C.H. Internal derangements of the temporomandibular joint. Pathological variations. *Arch Otolaryngol Head Neck Surg* **115**, 469-477 (1989).

35. Wu, Y. et al. The pilot study of fibrin with temporomandibular joint derived synovial stem cells in repairing TMJ disc perforation. *Biomed Res Int* **2014**, 454021 (2014).

36. Shen, P. et al. Magnetic resonance imaging applied to the diagnosis of perforation of the temporomandibular joint. *J Craniomaxillofac Surg* **42**, 874-878 (2014).

37. Murphy, M.K., Arzi, B., Prouty, S.M., Hu, J.C. & Athanasiou, K.A. Neocartilage integration in temporomandibular joint discs: physical and enzymatic methods. *J R Soc Interface* **12** (2015).

38. Milam, S.B. Failed implants and multiple operations. *Oral Surg Oral Med Oral Pathol Oral Radiol Endod* **83**, 156-162 (1997).

39. Liu, X.M. et al. Correlation between disc displacements and locations of disc perforation in the temporomandibular joint. *Dentomaxillofac Radiol* **39**, 149-156 (2010).

40. Kuribayashi, A., Okochi, K., Kobayashi, K. & Kurabayashi, T. MRI findings of temporomandibular joints with disk perforation. *Oral Surg Oral Med Oral Pathol Oral Radiol Endod* **106**, 419-425 (2008).

41. Miloro, M. & Henriksen, B. Discectomy as the primary surgical option for internal derangement of the temporomandibular joint. *Journal of Oral and Maxillofacial Surgery* **68**, 782-789 (2010).

42. Detamore, M.S. & Athanasiou, K.A. Motivation, characterization, and strategy for tissue engineering the temporomandibular joint disc. *Tissue engineering* **9**, 1065-1087 (2003).

43. Glaros, A.G. & Burton, E. Parafunctional clenching, pain, and effort in temporomandibular disorders. *J Behav Med* **27**, 91-100 (2004).

44. Mercuri, L.G. The use of alloplastic prostheses for temporomandibular joint reconstruction. *J Oral Maxillofac Surg* **58**, 70-75 (2000).

45. Sharma, H., Chowdhury, S., Navaneetham, A., Upadhyay, S. & Alam, S. Costochondral Graft as Interpositional material for TMJ Ankylosis in Children: A Clinical Study. *J Maxillofac Oral Surg* **14**, 565-572 (2015).

46. Kumar, D., Rajan, G., Raman, U. & Varghese, J. Autogenous Reconstructive Modalities of TMJ Ankylosis-A Retrospective Analysis of 45 Cases. *J Maxillofac Oral Surg* **13**, 359-365 (2014).

47. Sahoo, N.K., Tomar, K., Kumar, A. & Roy, I.D. Selecting reconstruction option for TMJ ankylosis: a surgeon's dilemma. *J Craniofac Surg* **23**, 1796-1801 (2012).

48. Zhang, X.H. et al. Simultaneous costochondral graft and distraction osteogenesis in unilateral TMJ ankylosis associated with mandibular retrognathia and asymmetry. *J Craniofac Surg* **23**, 682-684 (2012).

49. Mercuri, L.G. & Giobbie-Hurder, A. Long-term outcomes after total alloplastic temporomandibular joint reconstruction following exposure to failed materials. *J Oral Maxillofac Surg* **62**, 1088-1096 (2004).

50. Quinn, P. Pain management in the multiply operated temporomandibular joint patient. *J Oral Maxillofac Surg* **58**, 12-14 (2000).

51. Sidebottom, A.J. & Salha, R. Management of the temporomandibular joint in rheumatoid disorders. *Br J Oral Maxillofac Surg* **51**, 191-198 (2013).

52. Mercuri, L.G. Avoiding and managing temporomandibular joint total joint replacement surgical site infections. *J Oral Maxillofac Surg* **70**, 2280-2289 (2012).

53. Henry, C.H. & Wolford, L.M. Treatment outcomes for temporomandibular joint reconstruction after Proplast-Teflon implant failure. *J Oral Maxillofac Surg* **51**, 352-358; discussion 359-360. (1993).

54. Smith, M.H. et al. Computed tomography-based tissue-engineered scaffolds in craniomaxillofacial surgery. *Int J Med Robot* **3**, 207-216 (2007).

55. Almarza, A.J., Hagandora, C.K. & Henderson, S.E. Animal models of temporomandibular joint disorders: implications for tissue engineering approaches. *Annals of biomedical engineering* **39**, 2479-2490 (2011).

56. Hagandora, C. & Almarza, A. TMJ Disc Removal Comparison between Pre-clinical Studies and Clinical Findings. *Journal of dental research*, 0022034512453324 (2012).

57. Highley, C.B., Rodell, C.B. & Burdick, J.A. Direct 3D printing of shear‐thinning hydrogels into self‐healing hydrogels. *Advanced Materials* **27**, 5075-5079 (2015).

58. Trachtenberg, J.E. et al. Open‐source three‐dimensional printing of biodegradable polymer scaffolds for tissue engineering. *Journal of Biomedical Materials Research Part A* **102**, 4326-4335 (2014).

59. Billiet, T., Vandenhaute, M., Schelfhout, J., Van Vlierberghe, S. & Dubruel, P. A review of trends and limitations in hydrogel-rapid prototyping for tissue engineering. *Biomaterials* **33**, 6020-6041 (2012).

60. Levett, P.A. et al. A biomimetic extracellular matrix for cartilage tissue engineering centered on photocurable gelatin, hyaluronic acid and chondroitin sulfate. *Acta biomaterialia* **10**, 214-223 (2014).

61. Giannitelli, S., Mozetic, P., Trombetta, M. & Rainer, A. Combined additive manufacturing approaches in tissue engineering. *Acta biomaterialia* **24**, 1-11 (2015).

62. Klotz, B.J., Gawlitta, D., Rosenberg, A.J., Malda, J. & Melchels, F.P. Gelatin-methacryloyl hydrogels: towards biofabrication-based tissue repair. *Trends in biotechnology* **34**, 394-407 (2016).

63. Placone, J.K. et al. Development and characterization of a 3D printed, keratin-based hydrogel. *Annals of biomedical engineering* **45**, 237-248 (2017).

64. Zhu, W. et al. 3D printing of functional biomaterials for tissue engineering. *Current opinion in biotechnology* **40**, 103-112 (2016).

65. Zhu, J. & Marchant, R.E. Design properties of hydrogel tissue-engineering scaffolds. *Expert review of medical devices* **8**, 607-626 (2011).

66. Chimene, D., Lennox, K.K., Kaunas, R.R. & Gaharwar, A.K. Advanced bioinks for 3D printing: A materials science perspective. *Annals of biomedical engineering* **44**, 2090-2102 (2016).

67. Malda, J. et al. 25th anniversary article: engineering hydrogels for biofabrication. *Advanced Materials* **25**, 5011-5028 (2013).

68. Osterbur, L.W. (University of Illinois at Urbana-Champaign, 2013).

69. Sutherland, A.J. et al. Decellularized cartilage may be a chondroinductive material for osteochondral tissue engineering. *PLoS One* **10**, e0121966 (2015).

70. Pati, F. et al. Printing three-dimensional tissue analogues with decellularized extracellular matrix bioink. *Nature communications* **5** (2014).

71. Schwarz, S. et al. Decellularized cartilage matrix as a novel biomatrix for cartilage tissue-engineering applications. *Tissue engineering Part A* **18**, 2195-2209 (2012).

72. Beck, E.C. et al. Enabling surgical placement of hydrogels through achieving paste-like rheological behavior in hydrogel precursor solutions. *Annals of biomedical engineering* **43**, 2569-2576 (2015).

73. Mergy, J., Fournier, A., Hachet, E. & Auzély‐Velty, R. Modification of polysaccharides via thiol‐ene chemistry: A versatile route to functional biomaterials. *Journal of Polymer Science Part A: Polymer Chemistry* **50**, 4019-4028 (2012).

74. Tomlins, P. Characterisation and Design of Tissue Scaffolds. (Woodhead Publishing, 2015).

75. Wijnen, B., Hunt, E.J., Anzalone, G.C. & Pearce, J.M. Open-source syringe pump library. *PloS one* **9**, e107216 (2014).

76. Puetzer, J.L., Petitte, J.N. & Loboa, E.G. Comparative review of growth factors for induction of three-dimensional in vitro chondrogenesis in human mesenchymal stem cells isolated from bone marrow and adipose tissue. *Tissue Engineering Part B: Reviews* **16**, 435-444 (2010).

77. Caliari, S.R. & Burdick, J.A. A practical guide to hydrogels for cell culture. *Nature methods* **13**, 405-414 (2016).

78. Sutherland, A.J., Converse, G.L., Hopkins, R.A. & Detamore, M.S. The bioactivity of cartilage extracellular matrix in articular cartilage regeneration. *Advanced healthcare materials* **4**, 29-39 (2015).

79. Daly, K.A., Stewart-Akers, A.A., Cordero, K., Johnson, S.A. & Badylak, S.F. The effect of the αGal epitope in the response to ECM in a nonhuman primate model (141.26). *The Journal of Immunology* **182**, 141.126-141.126 (2009).

80. Kuroda, S. et al. Biomechanical and biochemical characteristics of the mandibular condylar cartilage. *Osteoarthritis and Cartilage* **17**, 1408-1415 (2009).

81. Beck, E.C. et al. Chondroinductive hydrogel pastes composed of naturally derived devitalized cartilage. *Annals of biomedical engineering* **44**, 1863-1880 (2016).

82. Boere, K.W. et al. Covalent attachment of a three-dimensionally printed thermoplast to a gelatin hydrogel for mechanically enhanced cartilage constructs. *Acta biomaterialia* **10**, 2602-2611 (2014).

83. Bryant, S.J. & Anseth, K.S. Hydrogel properties influence ECM production by chondrocytes photoencapsulated in poly (ethylene glycol) hydrogels. *Journal of Biomedical Materials Research Part A* **59**, 63-72 (2002).

84. Sophia Fox, A.J., Bedi, A. & Rodeo, S.A. The basic science of articular cartilage: structure, composition, and function. *Sports health* **1**, 461-468 (2009).

85. Akiyama, H. Control of chondrogenesis by the transcription factor Sox9. *Modern Rheumatology* **18**, 213-219 (2008).

86. Wolford, L.M. & Mehra, P. in Baylor University Medical Center. Proceedings, Vol. 13 135 (Baylor University Medical Center, 2000).

87. Vacanti, J.P. & Langer, R. Tissue engineering: the design and fabrication of living replacement devices for surgical reconstruction and transplantation. *The lancet* **354**, S32-S34 (1999).

88. Houben, A. et al. Indirect rapid prototyping: opening up unprecedented opportunities in scaffold design and applications. *Annals of biomedical engineering* **45**, 58-83 (2017).

89. Sears, N.A., Seshadri, D.R., Dhavalikar, P.S. & Cosgriff-Hernandez, E. A review of three-dimensional printing in tissue engineering. *Tissue Engineering Part B: Reviews* **22**, 298-310 (2016).

90. Holmes, B., Zhu, W., Li, J., Lee, J.D. & Zhang, L.G. Development of novel three-dimensional printed scaffolds for osteochondral regeneration. *Tissue Engineering Part A* **21**, 403-415 (2014).

91. Zhang, W. et al. Cartilage repair and subchondral bone migration using 3D printing osteochondral composites: a one-year-period study in rabbit trochlea. *BioMed research international* **2014** (2014).

92. Fedorov, A. et al. 3D Slicer as an image computing platform for the Quantitative Imaging Network. *Magnetic resonance imaging* **30**, 1323-1341 (2012).

93. Murphy, C.M., Haugh, M.G. & O'Brien, F.J. The effect of mean pore size on cell attachment, proliferation and migration in collagen–glycosaminoglycan scaffolds for bone tissue engineering. *Biomaterials* **31**, 461-466 (2010).

94. Jeong, C.G. & Atala, A. in Engineering Mineralized and Load Bearing Tissues 3-14 (Springer, 2015).

95. Kazmer, D. et al. A PROTOCOL FOR FILAMENT PRODUCTION AND USE IN FUSED DEPOSITION MODELING.

96. Zopf, D.A. et al. Computer Aided–Designed, 3-Dimensionally Printed Porous Tissue Bioscaffolds for Craniofacial Soft Tissue Reconstruction. *Otolaryngology--Head and Neck Surgery* **152**, 57-62 (2015).

97. Steuben, J., Van Bossuyt, D.L. & Turner, C. in ASME 2015 International Design Engineering Technical Conferences and Computers and Information in Engineering Conference V004T005A050-V004T005A050 (American Society of Mechanical Engineers, 2015).

98. Lee, J.-Y., Choi, B., Wu, B. & Lee, M. Customized biomimetic scaffolds created by indirect three-dimensional printing for tissue engineering. *Biofabrication* **5**, 045003 (2013).

Appendix: Figures

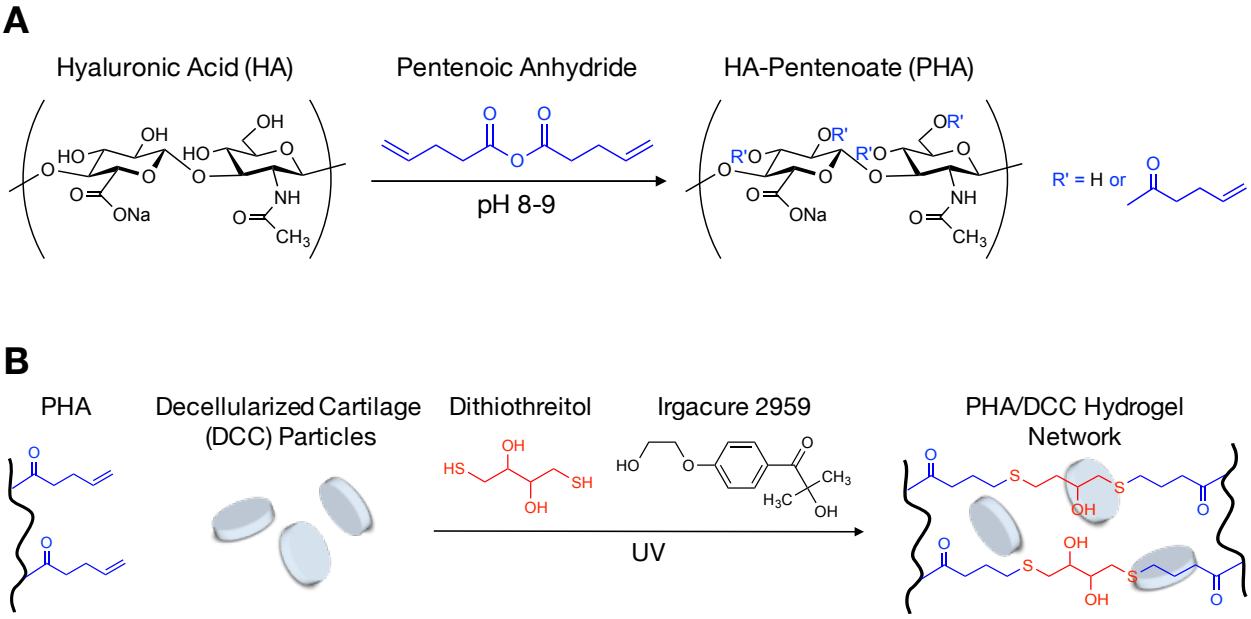

Figure 3.1. A) Schematic of pentenoate functionalization of hyaluronic acid. B) Hydrogel formation of solubilized PHA containing DCC microparticles via photoinitiated radical thiol-ene 'click' chemistry.

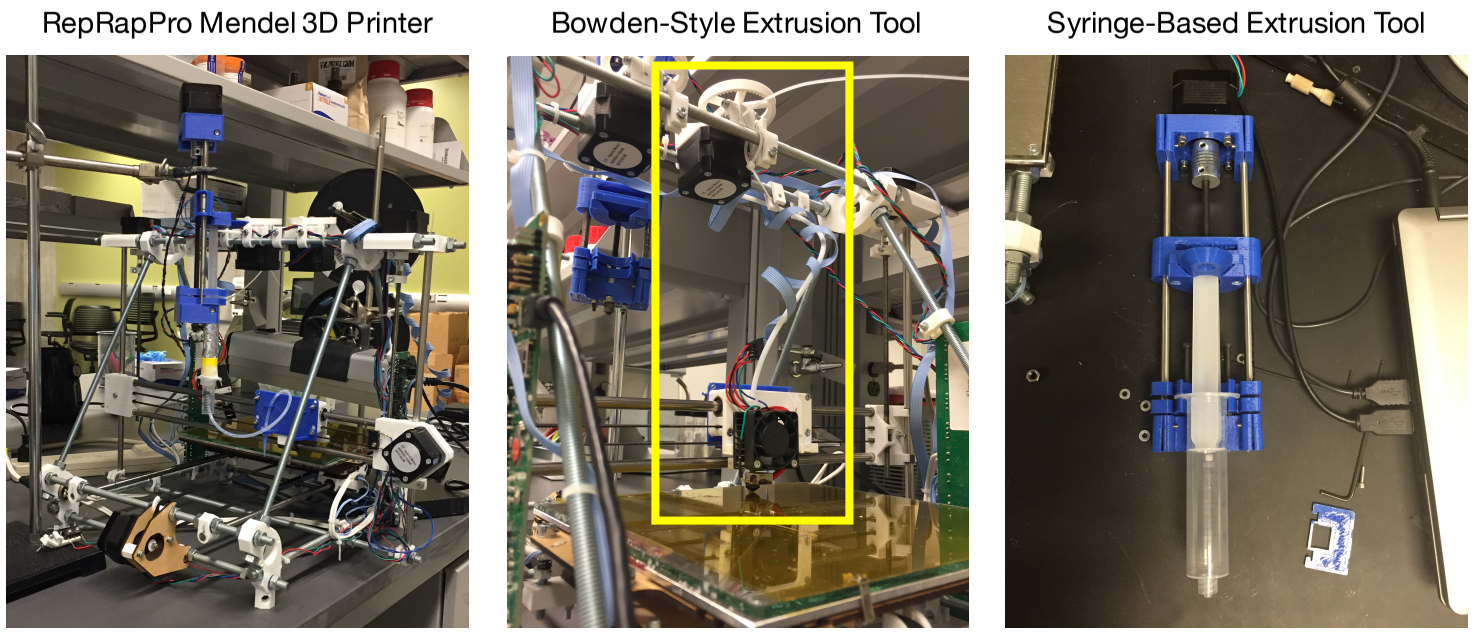

Figure 3.2. RepRapPro 3D Printer equipped with Bowden-style and syringe-based extrusion tools for fused deposition modeling and direct ink writing, respectively. In addition, a UV light source suspended over the build plate initates photocrosslinking of hydrogel inks.

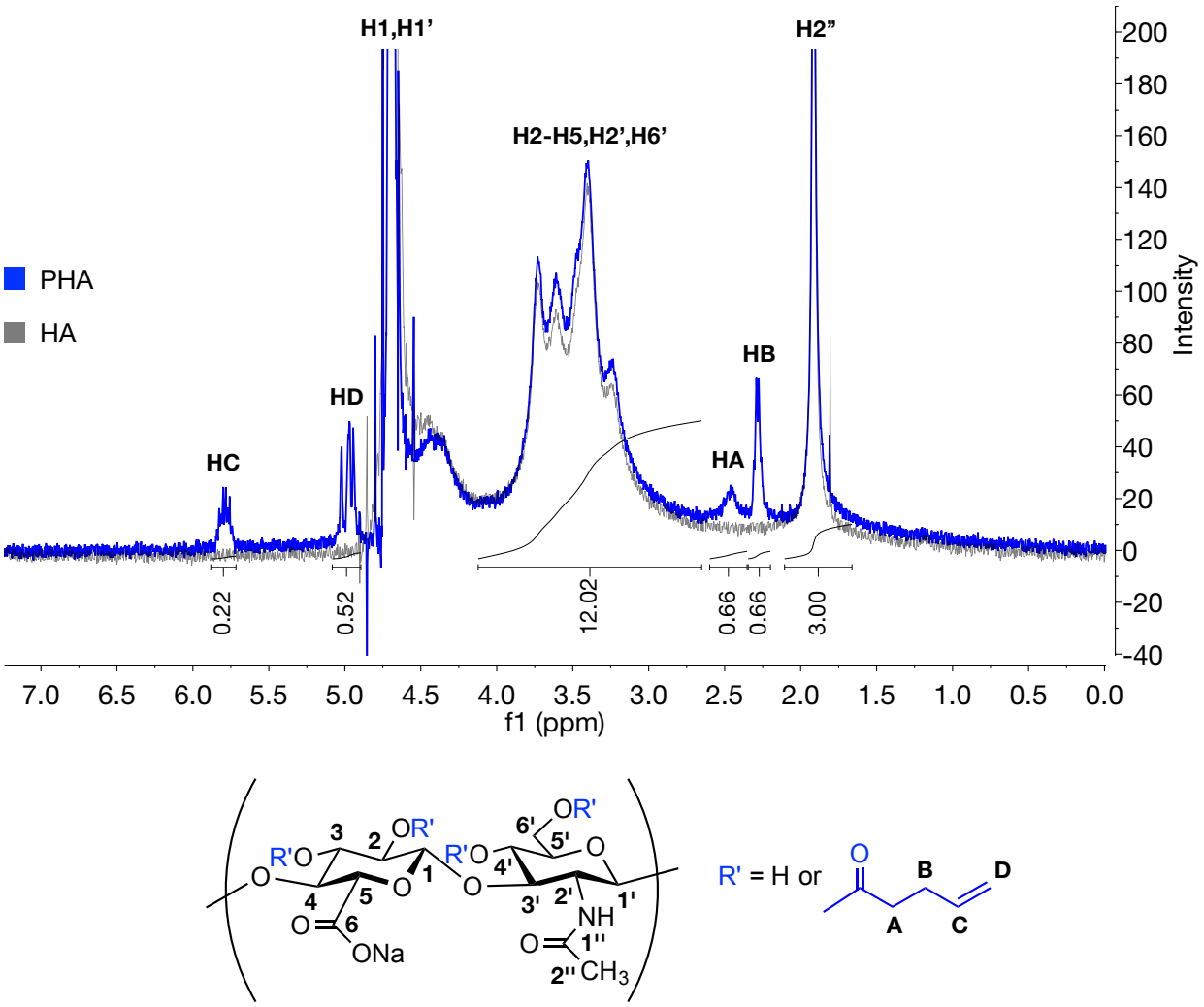

Figure 3.3. Confirmation of pentenoate functionalization of HA. ^{H}NMR spectra for pentenoate-modified hyaluronic acid (PHA) compared to pure hyaluronic acid (HA). Peaks at 2.25, 2.5, 5.0 and 5.75 are indicative of pentenoate functionalization. The degree of functionalization was determined by comparing the intensities of the peaks located at 1.75 and 5.75 ppm (i.e., the relative amount of H2'' protons to the amount of HC protons).

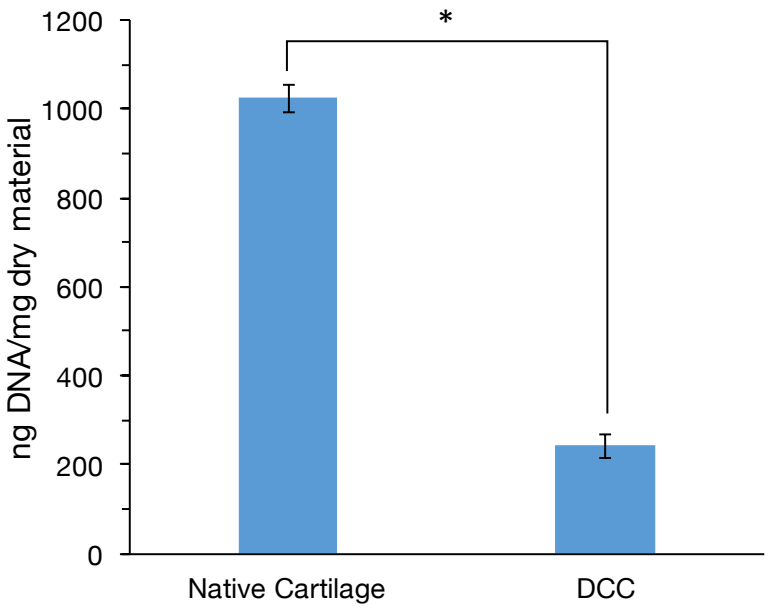

Figure 3.4. Confirmation of cartilage decellularization. Fluorometric dsDNA quantification of cryoground native porcine cartilage and decellularized cartilage (DCC). Results are reported as the mean ± standard deviation. * indicates statistically significant difference among groups ($p<0.05$).

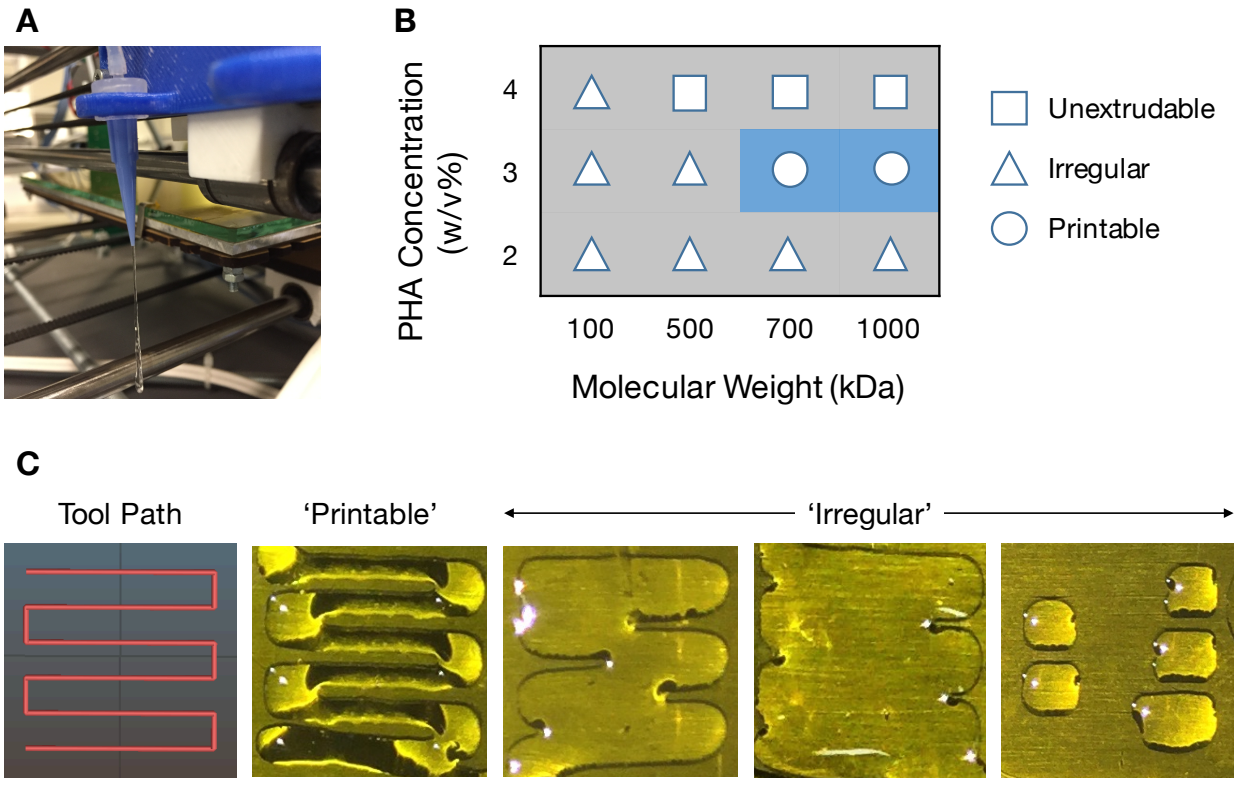

Figure 3.5. Printability tests of PHA hydrogel inks with varied concentrations (2, 3 and 4 w/v%) and molecular weights of PHA (100, 500, 700 and 1000 kDa). A) Image of the extrusion of 3 w/v% 1MDa-PHA hydrogel ink as a stable filament strand from an 18-gauge dispensing tip. B) Summary of the printability of various PHA hydrogel ink formulations. C) Depiction of single-layer 1 cm x 1 cm test print and representative images of various PHA hydrogel ink depositions to convey what was deemed 'printable' and what was deemed 'irregular'.

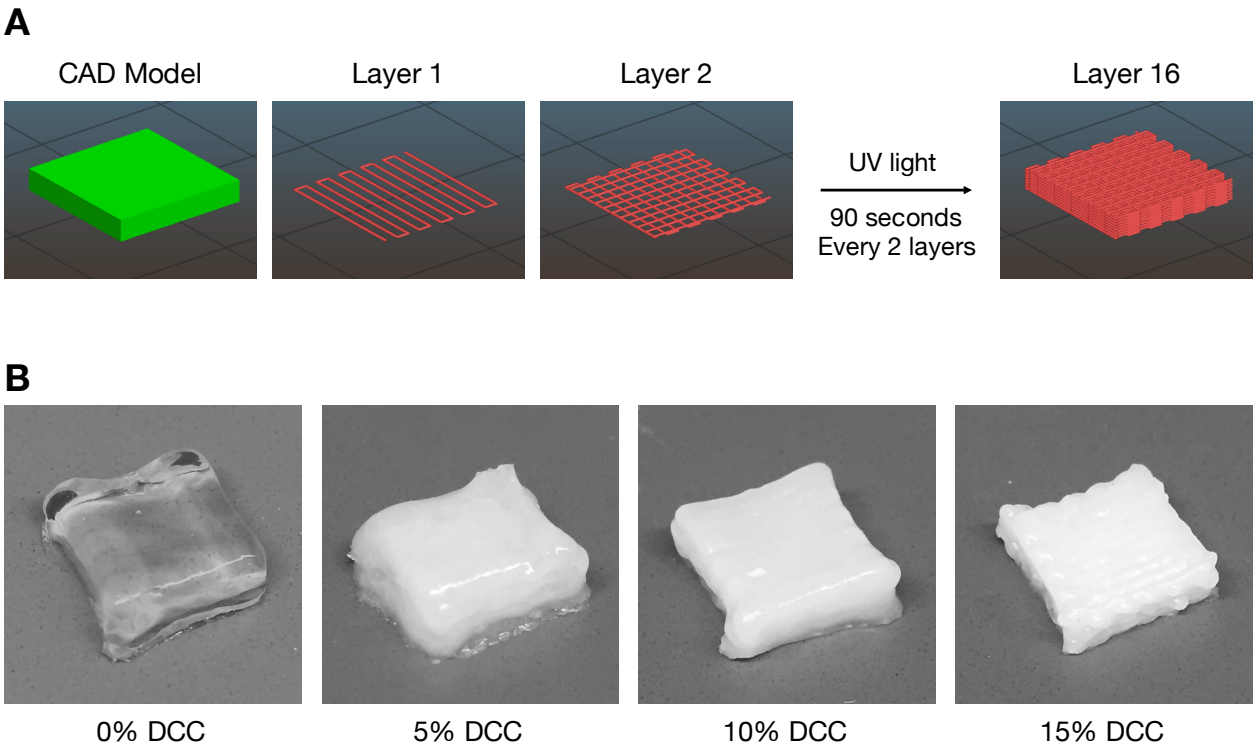

Figure 3.6. Scheme for printing hydrogel layers, and images of 3D-printed PHA/DCC hydrogels. A) Depiction of 3D-printed 16-layer hydrogel assembly. The CAD model (green) is converted into user-generated tool paths (red) with slicing software. Hydrogel ink is deposited with 0-90° rectilinear infill patterns. After every 2 layers, the printed structure is cured with UV light for 90 seconds until the final structure is realized. B) Macroscopic images of 16-layered, 3D-printed PHA hydrogels with 0, 5, 10 and 15 w/v% DCC microparticles constructed with the syringe-based extrusion tool. The base of the hydrogels are 1 cm x 1 cm.

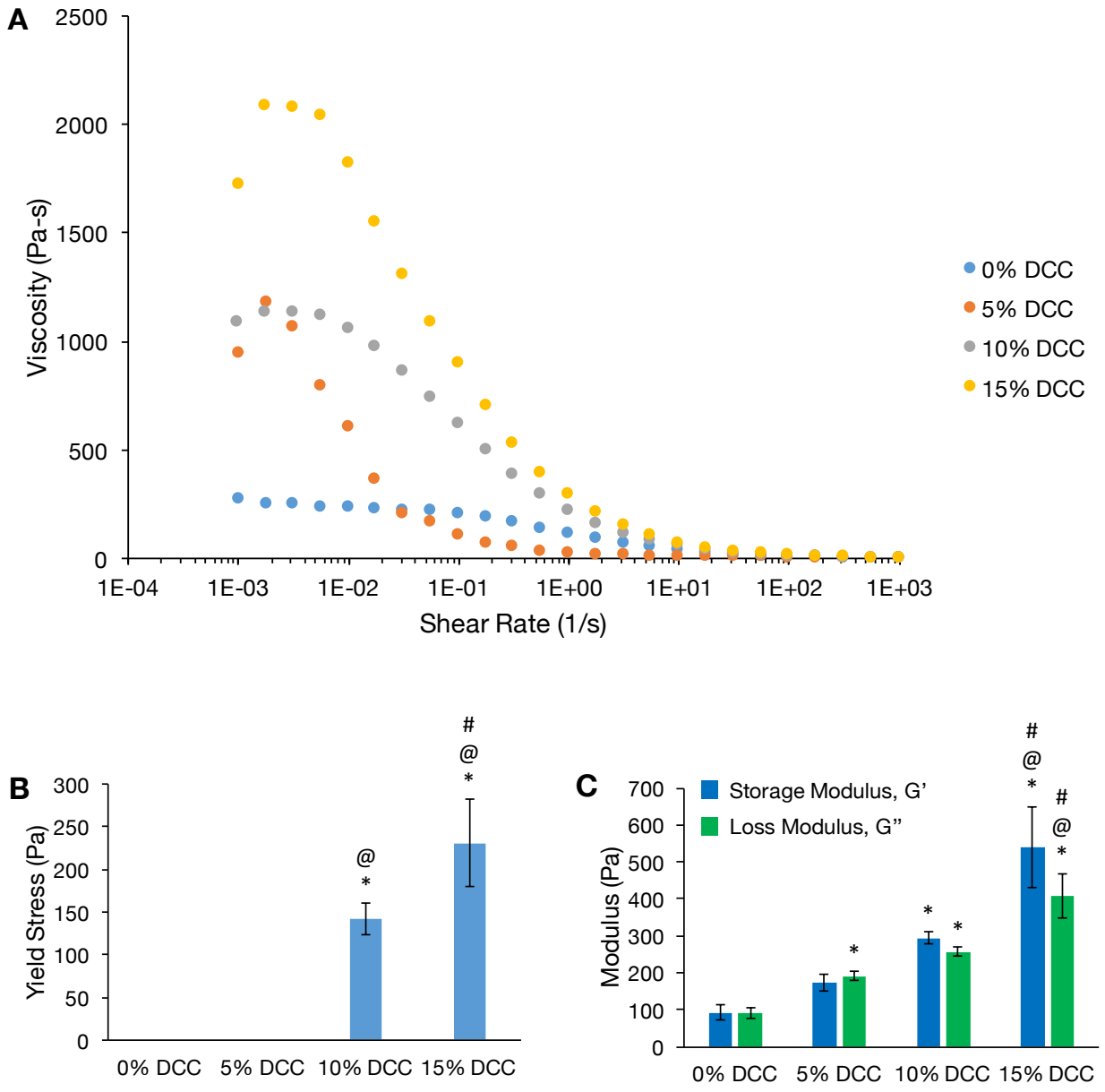

Figure 3.7. Rheological properties of various hydrogel formulations. A) Representative flow curves of PHA/DCC precursor mixtures. B) Yield stress and C) Storage and loss moduli reported as mean ± standard deviation in Pascals for PHA hydrogel precursor mixtures containing 0, 5, 10 and 15% DCC particles. * denotes statistically significant differences from 0% DCC group, @ denotes differences from 5% DCC group, # denotes differences from 10% DCC group ($p<0.05$).

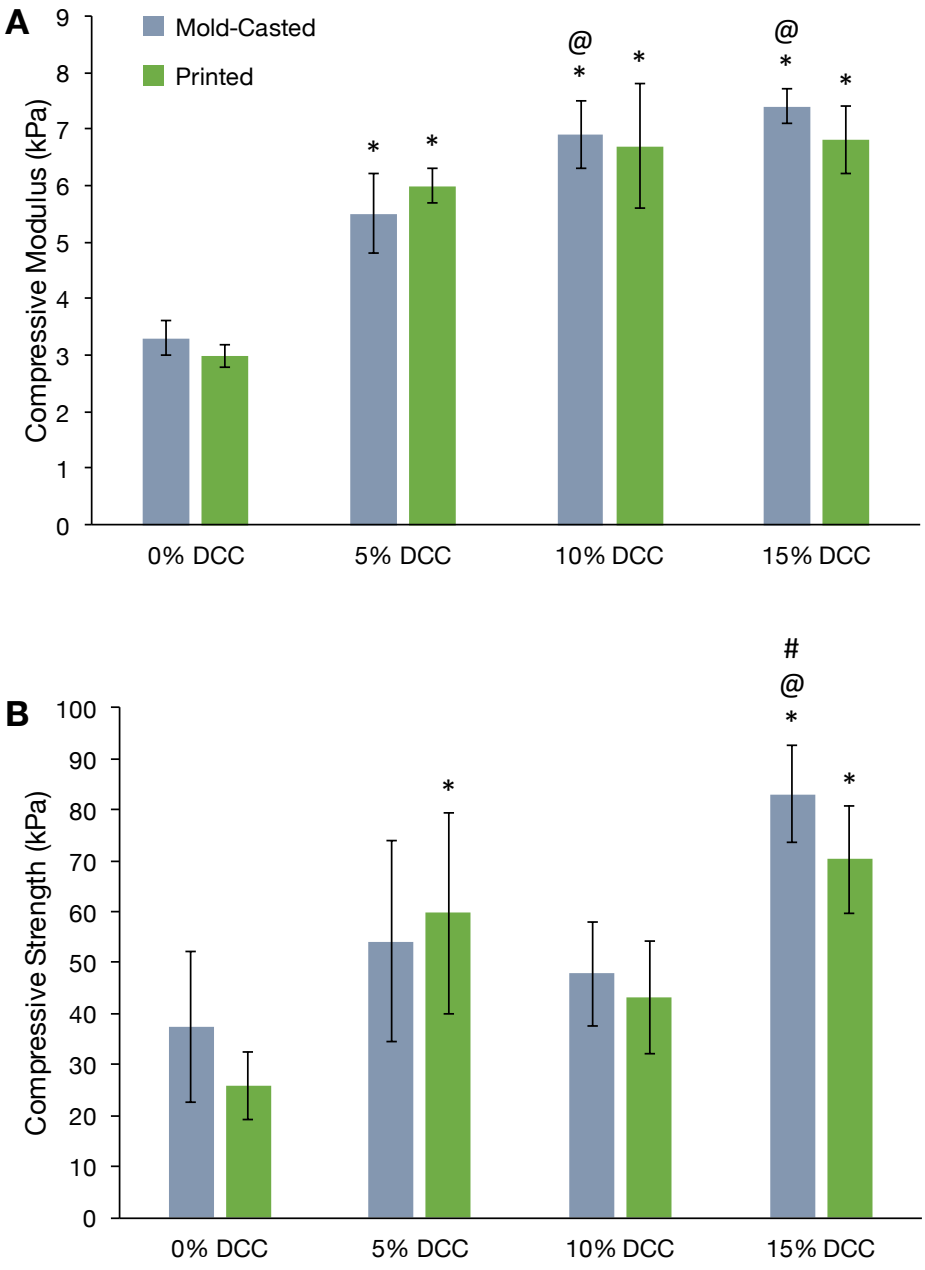

Figure 3.8. Effect of DCC enrichment and fabrication method on mechanical properties of PHA hydrogel. A) Compressive stiffness and B) Compressive strength reported as mean ± standard deviation in units of kPa for PHA hydrogels containing 0, 5, 10 and 15% DCC microparticles fabricated by mold-casting (gray) and 3D-printing (green) methods. No significant differences were found between mold-casted and 3D-printed gels with the same hydrogel formulation. * denotes statistically significant difference from 0% DCC group with same fabrication method, @ denotes difference from 5% DCC group with same fabrication method, # denotes difference from 10% DCC group with same fabrication method ($p<0.05$).

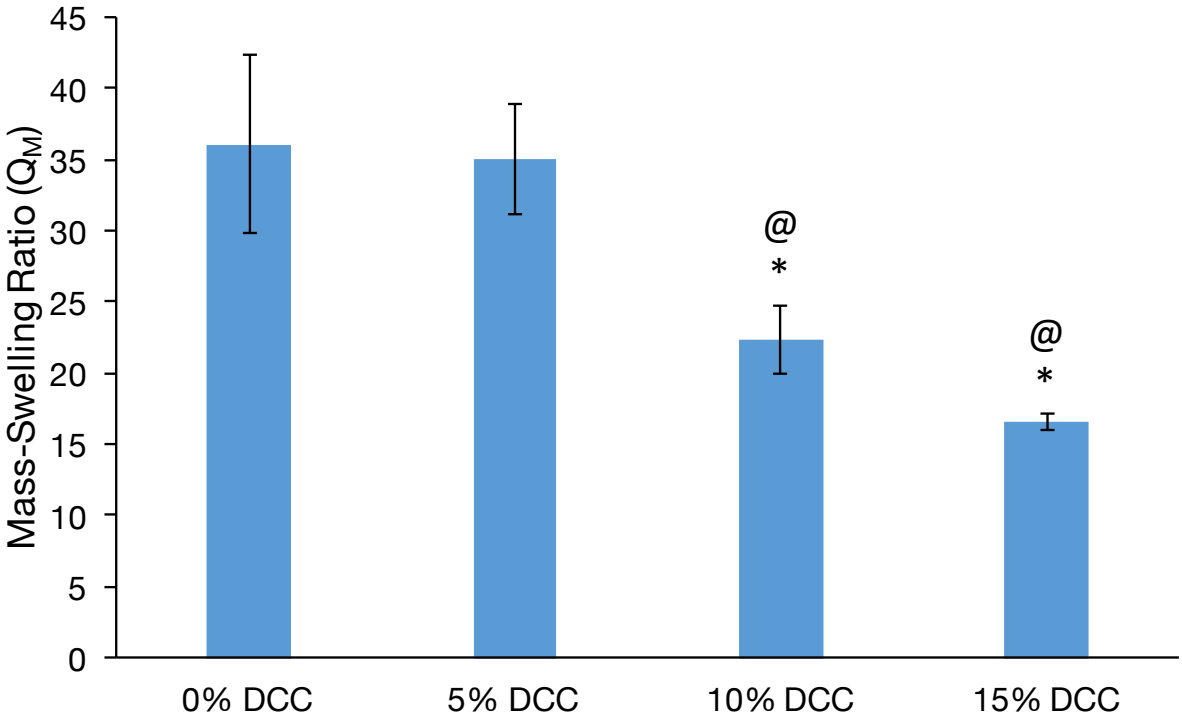

Figure 3.9. Mass-swelling ratio of PHA hydrogel with 0, 5, 10 and 15 w/v% DCC microparticles reported as mean ± standard deviation. * denotes statistically significant difference from 0% DCC group, @ denotes difference from 5% DCC group, # denotes difference from 10% DCC group ($p<0.05$).

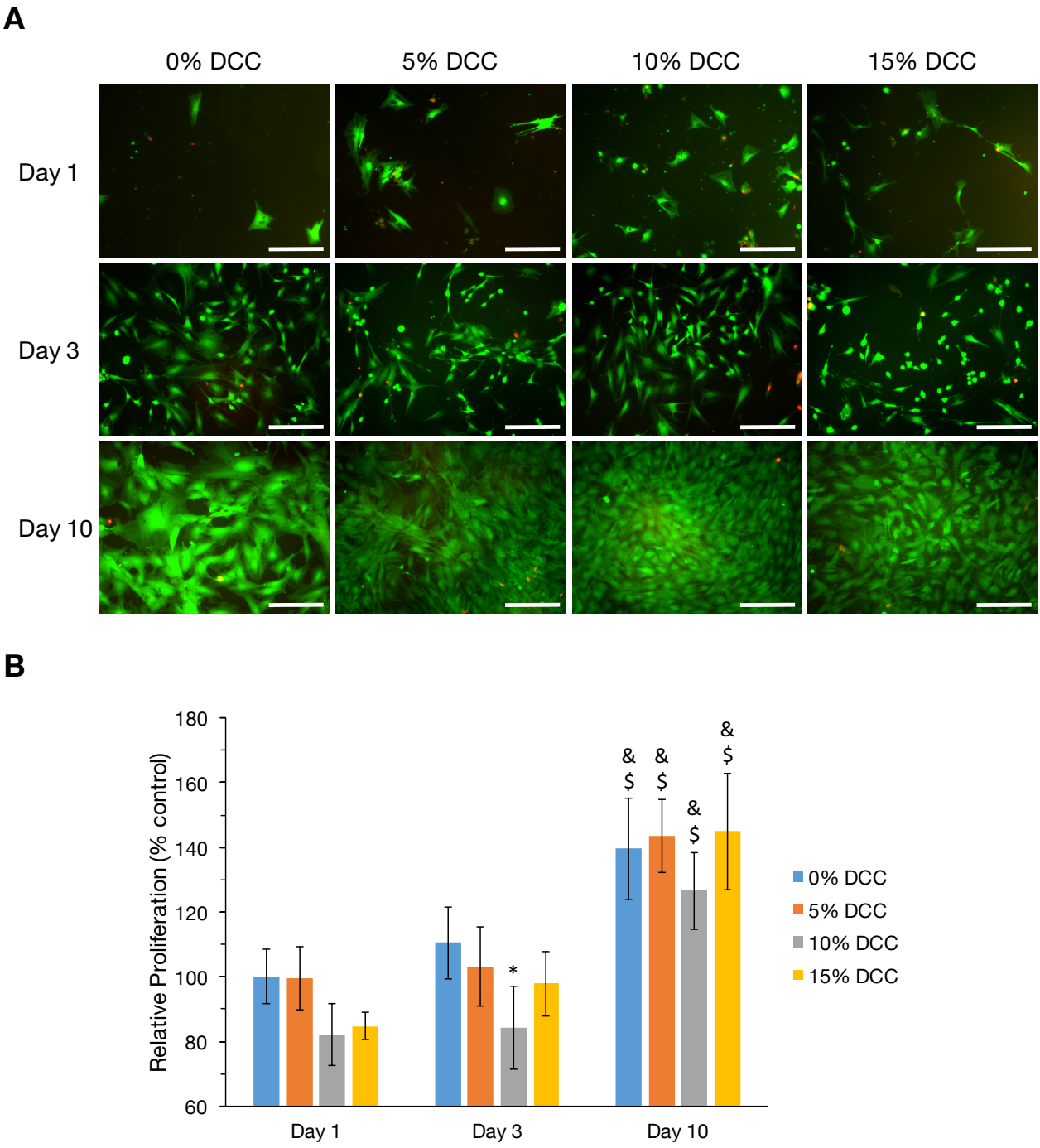

Figure 3.10. Cytocompatibility of the developed hydrogel. A) LIVE/DEAD cell imaging (scale bars are equal to 200 µm) and B) Relative proliferation of rat bone marrow stem cells seeded on PHA hydrogels containing various concentrations of DCC microparticles over 10 days in 2D culture. * denotes statistically significant difference from 0% DCC formulation at same time point, @ denotes difference from 5% DCC at same time point, # denotes difference from 10% DCC at same time point, $ denotes difference from same formulation group at day 1, and & denotes difference from same formulation group at week 2 ($p<0.05$).

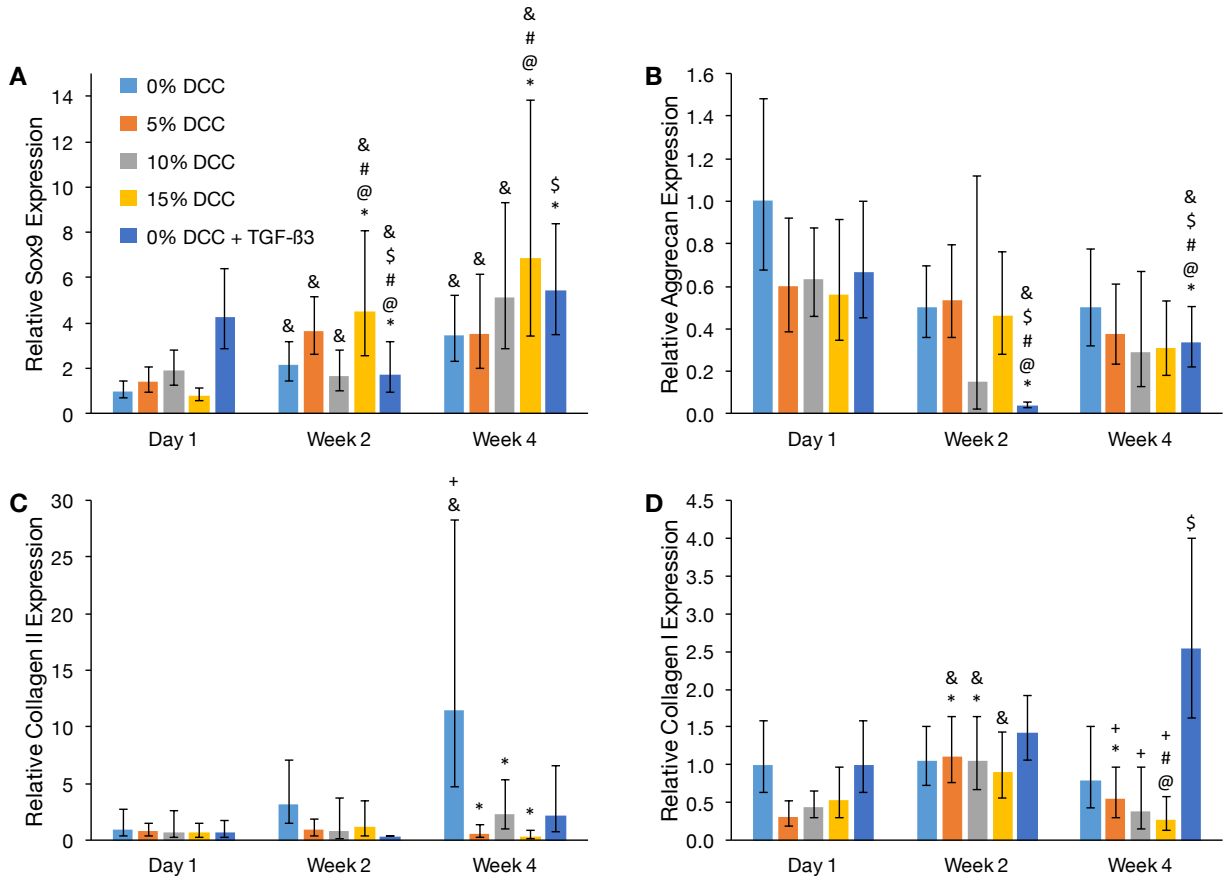

Figure 3.11. Relative expression levels of chondrogenic genes encoding for A) Sox9, B) Aggrecan, C) Collagen II, and of D) Collagen I, an osteogenic gene. * denotes statistically significant difference from negative control group (0% DCC formulation) at same time point, @ denotes difference from 5% DCC at same time point, # denotes difference from 10% DCC at same time point, $ denotes difference from 15% DCC at same time point, & denotes difference from same formulation group at day 1, and + denotes difference from same formulation group at week 2 ($p<0.05$).

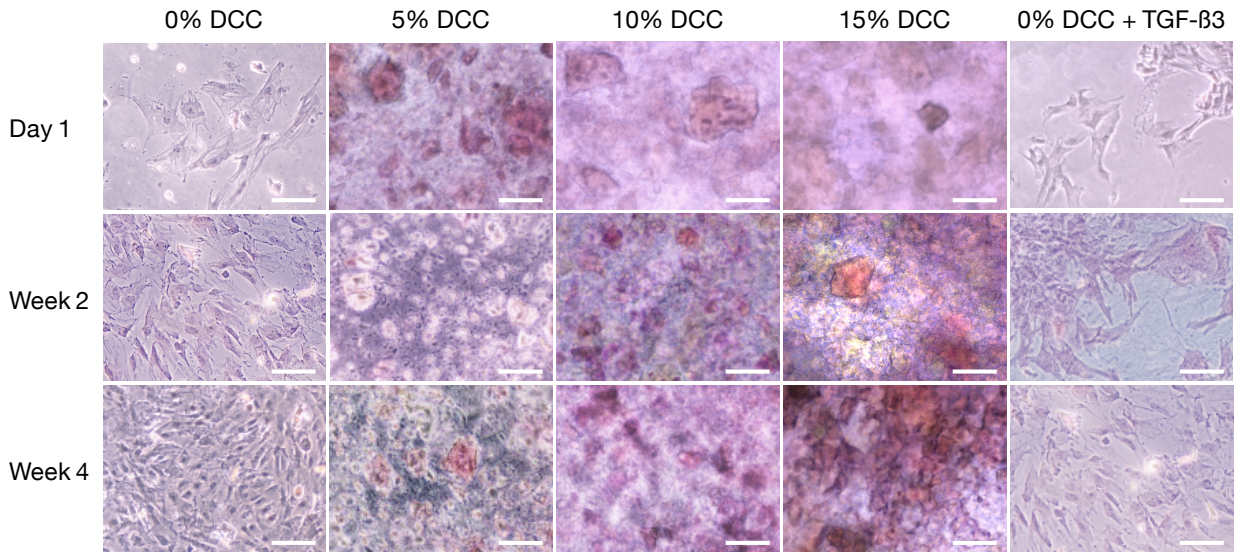

Figure 3.12. Hematoxylin and Eosin staining from day 1 to week 4 of PHA/DCC hydrogel formulations seeded with cells. The nuclei are stained dark purple and cellular cytoplasm is stained pink. The scale bars are equal to 100 μm.

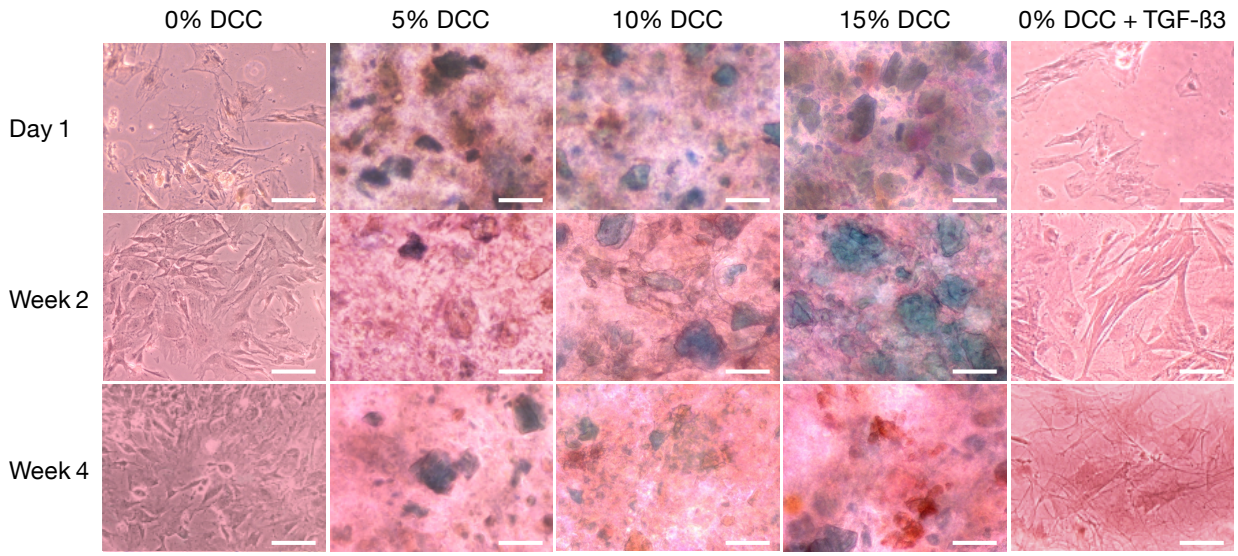

Figure 3.13. Safranin O and Fast Green stains of cells cultured on PHA hydrogels with various concentrations of DCC (5, 10 and 15%) compared to the negative (0% DCC) and positive control (0% DCC plus exogenous TGF-ß3 supplementation) over a four week period. Safranin O stains GAGs orange-red, and Fast Green stains noncollagenous materials green. The scale bars are equal to 100 µm.

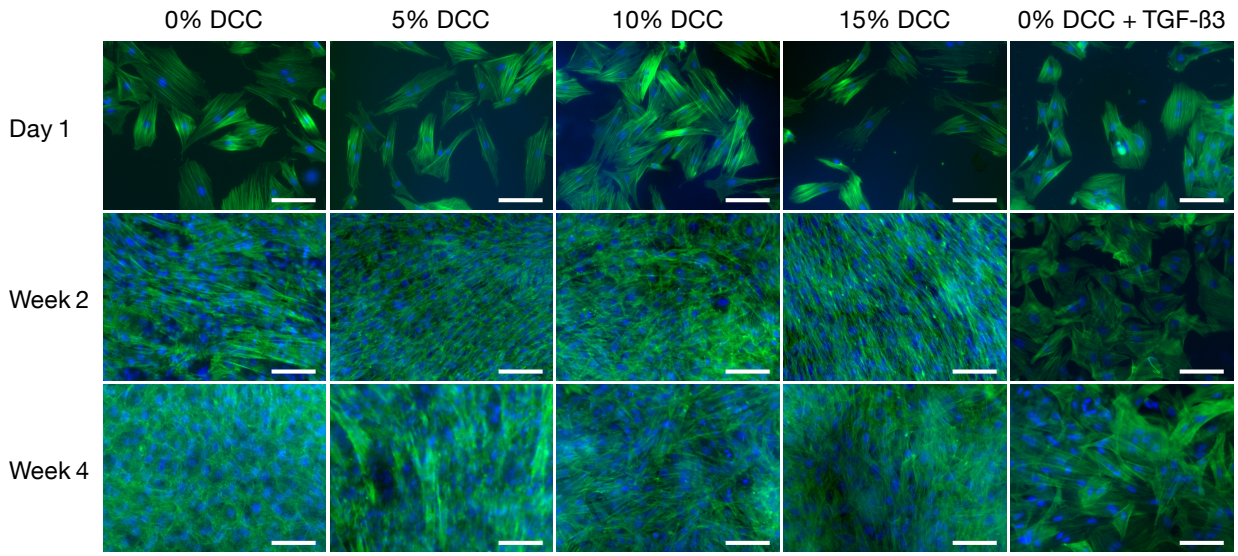

Figure 3.14. DAPI and phalloidin fluorescent staining of cells cultured on PHA/DCC hydrogel formulations from day 1 to week 4. Cellular F-actin is depicted in green and the nuclei are depicted in blue. The scale bars are equal to 100 µm.

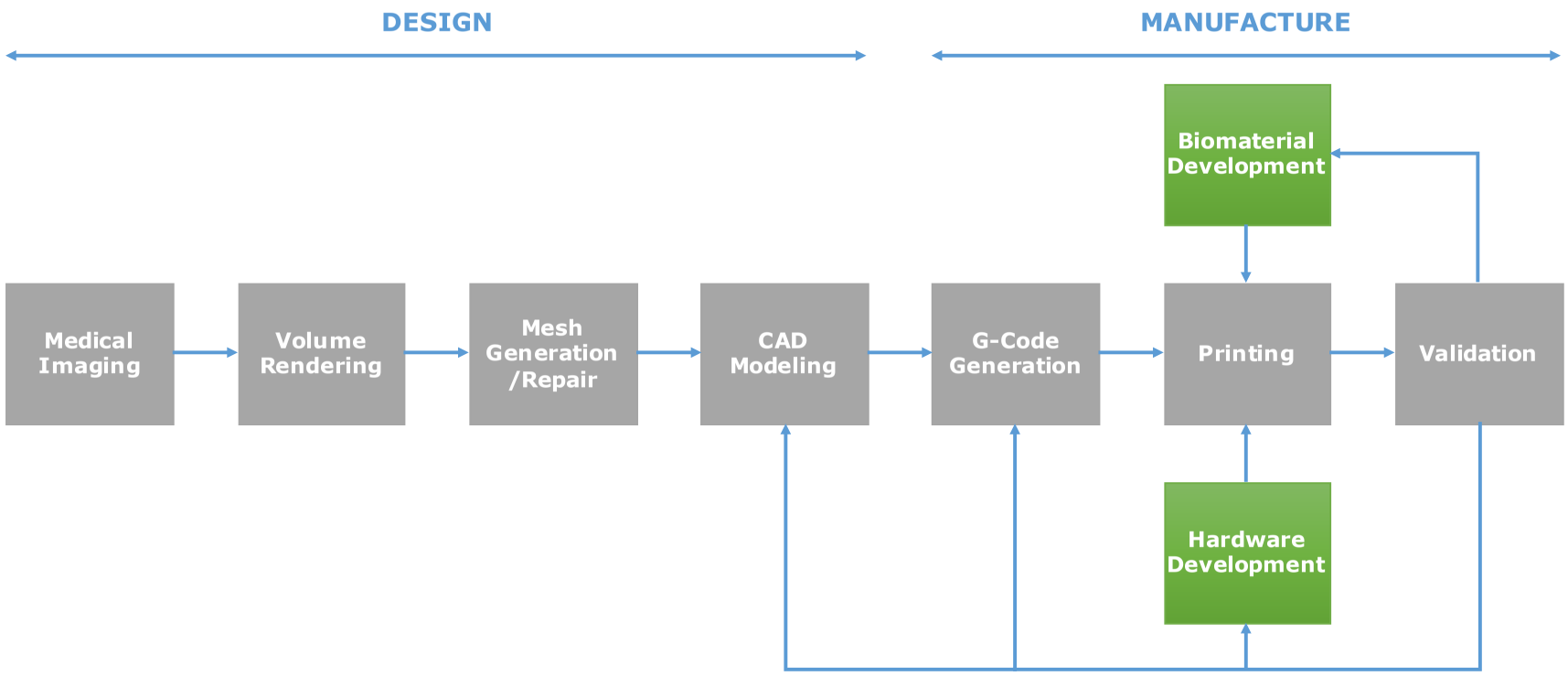

Figure 4.1. Process flow chart for the computer-aided design and manufacture of patient-specific scaffolds for tissue engineering including the interdependencies of biomaterial and hardware optimization.

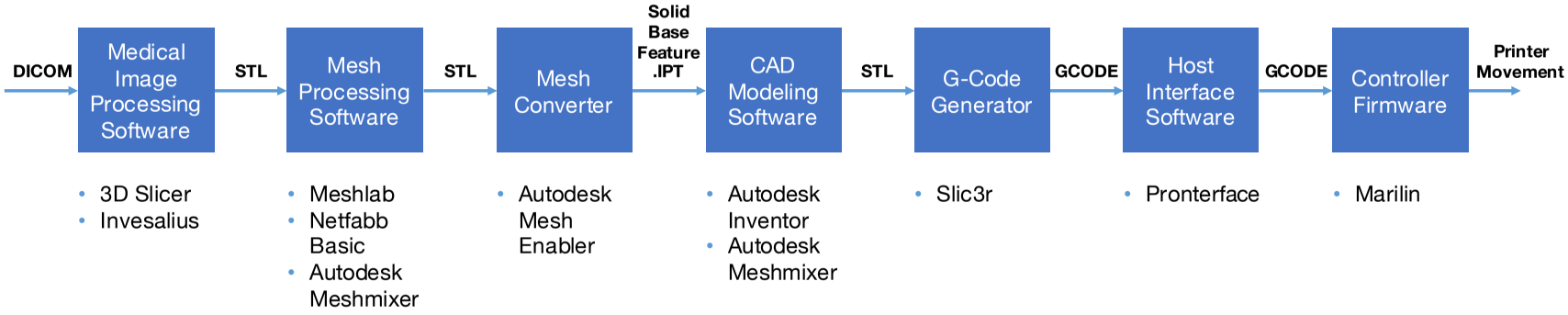

Figure 4.2. Software toolchain used to generate patient-specific scaffolds from medical imaging data. The open-source software programs used in this thesis are featured as bulleted lists below the software description boxes. The file format inputs and outputs are also provided.

A) Medical Imaging

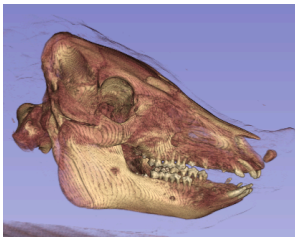

B) Volume Rendering

C) Mesh Generation/Repair

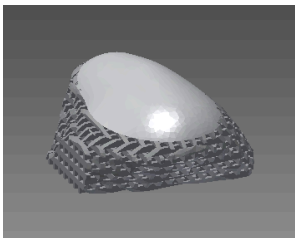

D) CAD Modeling

Figure 4.3. Computer-aided scaffold design process of the patient-specific osteochondral scaffold for mandibular condyle regeneration from CT scans of a hog head to a digital model of the bone and cartilage regions (shown in dark gray and light gray, respectively) of the scaffold.

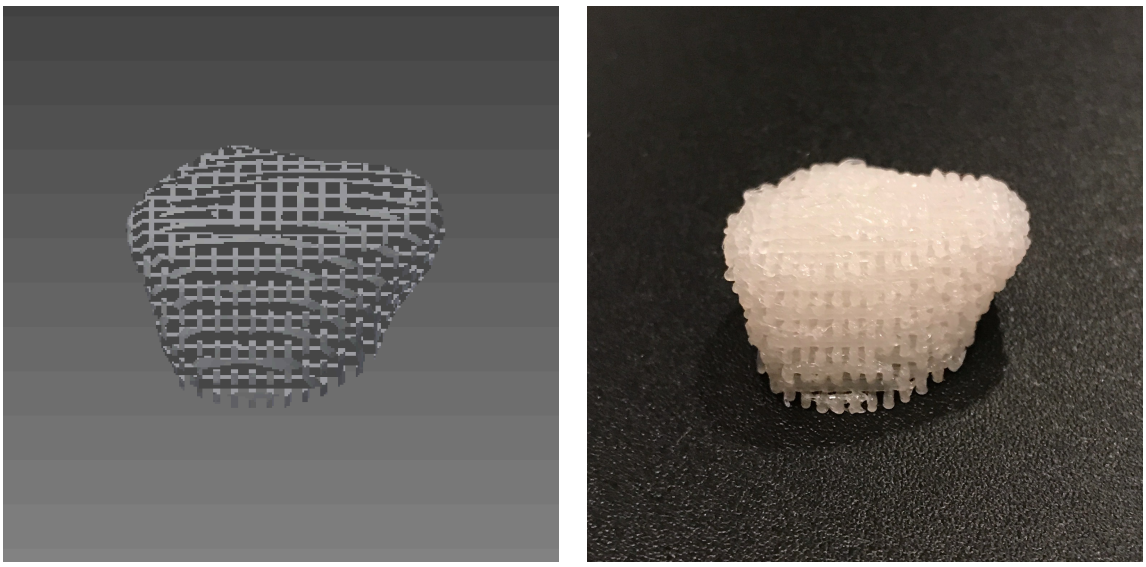

Figure 4.4. Bone-promoting scaffold region of the condylar process.

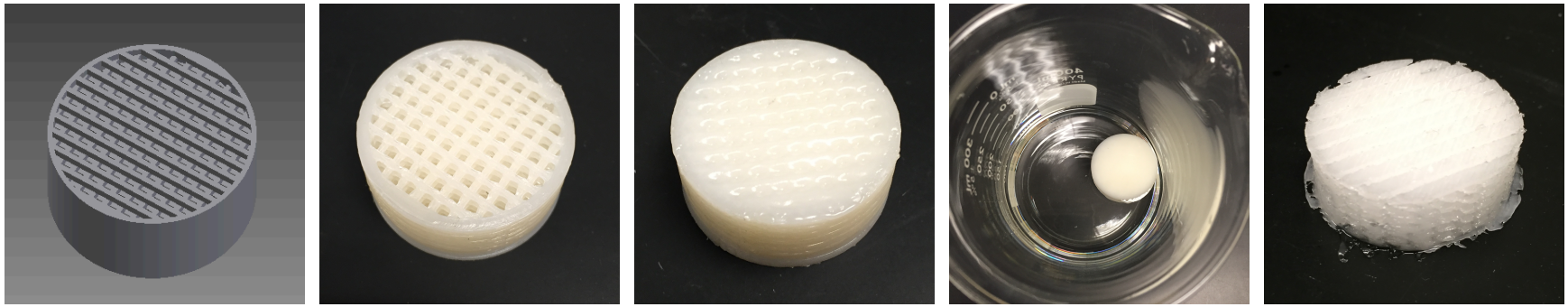

Figure 4.5. Indirect 3D printing of a PCL/HAnp scaffold.

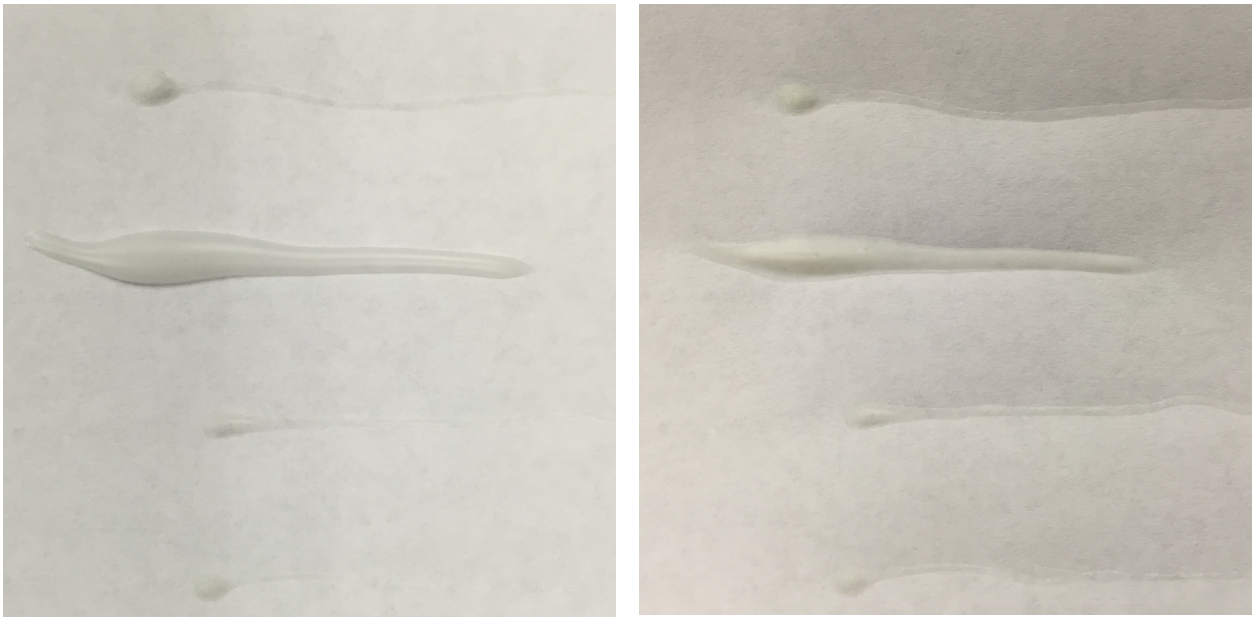

BEFORE SOLVENT EVAPORATION AFTER SOLVENT EVAPORATION

Figure 4.6. Solvent printing of PCL and 10 w/w% HAnp dissolved/suspended in DCM before and after solvent evaporation.